International Journal of Engineering Science 169 (2021) 103564

Contents lists available at ScienceDirect

International Journal of Engineering Science

journal homepage: www.elsevier.com/locate/ijengsci

A thermomechanical and photochemical description of the phase change process in roll-to-roll nanoimprinting lithography

J.P. Gomez-Constante, P.R. Pagilla, K.R. Rajagopal *

Department of Mechanical Engineering, Texas A&M University, College Station, United States of America

ARTICLE INFO

Keywords:
Roll-to-roll transport
Nanoimprinting lithography
Multiscale modeling
Viscoelastic material
Photochemical bonding
Mechanics of mixtures

ABSTRACT

In this paper, a model for the phase change process due to irradiation with an Ultraviolet (UV) light in a mold filled with a viscoelastic fluid in roll-to-roll nanoimprinting lithography is developed. Employing a thermomechanical approach, constitutive equations for the phase change of a mixture of viscoelastic fluid and solid constituents of the polymer are derived. A general model describing phase change that relates both thermomechanics and photochemistry is presented. A function defining the mass fractions of fluid and solid in the mixture is utilized in the thermomechanical description, and the governing equations for the evolution of the fluid and solid mixtures are obtained based on photochemical reactions under UV light. General properties and kinematic equations that impact phase change in terms of material properties and process parameters are obtained. A simplification of the model without sacrificing the underlying physics to make the problem amenable to analysis is put into place. The general model of phase transition is simplified by assuming that the gradient of the displacement, the strain and its time rate, are small; this results in an integro-differential quasilinear system of equations. A numerical scheme is proposed to solve the problem and results from the numerical simulations are presented and discussed.

1. Introduction

A comprehensive description of the phase change process in general terms started with the early work of Lamé and Clapeyron (1831), where solidification due to heat conduction was the driving catalyst for the phase change process. Based on their findings, a new class of models emerged for the Lamé–Clapeyron–Stefan problem, and results related to that problem are discussed in Beckermann, Diepers, Steinbach, Karma, and Tong (1999) and Rubinštein (2000). These models basically consider a general approach based on the heat equation with free boundaries that takes into account some thermodynamic aspects of heat conduction for the initial and boundary conditions, and mass flux via the Navier–Stokes equations (Gupta, 2017; Hu & Argyropoulos, 1996). A great deal of mathematical work has been carried out with regard to the problem of solidification and melting and a detailed account of the same with copious literature can be found in Bankoff (1964), Crank (1956), and Rubinštein (2000). On the physical side Avrami wrote a series of papers concerning the equations underlying the phenomenon of phase change (see Avrami, 1939, 1940, 1941). Baldoni and Rajagopal (1997) have also proposed a thermodynamics for solidification.

We should mention closely related papers wherein the same thermodynamic framework is used to develop constitutive relations when polymeric materials are undergoing phase change. Early studies of the same are due to Fasano, Kannan, Mancini, and Rajagopal (2007), Kannan, Rao, and Rajagopal (2002), and Rao and Rajagopal (2001, 2002). Some relevant later studies concern phase change in polymers that are light activated with the added property of having memory for certain preferred shapes (see Barot, Rao, &

* Corresponding author.
E-mail addresses: juanpablogomezc@tamu.edu (J.P. Gomez-Constante), ppagilla@tamu.edu (P.R. Pagilla), krajagopal@tamu.edu (K.R. Rajagopal).

https://doi.org/10.1016/j.ijengsci.2021.103564
Received 29 June 2021; Received in revised form 13 August 2021; Accepted 13 August 2021
Available online 8 September 2021

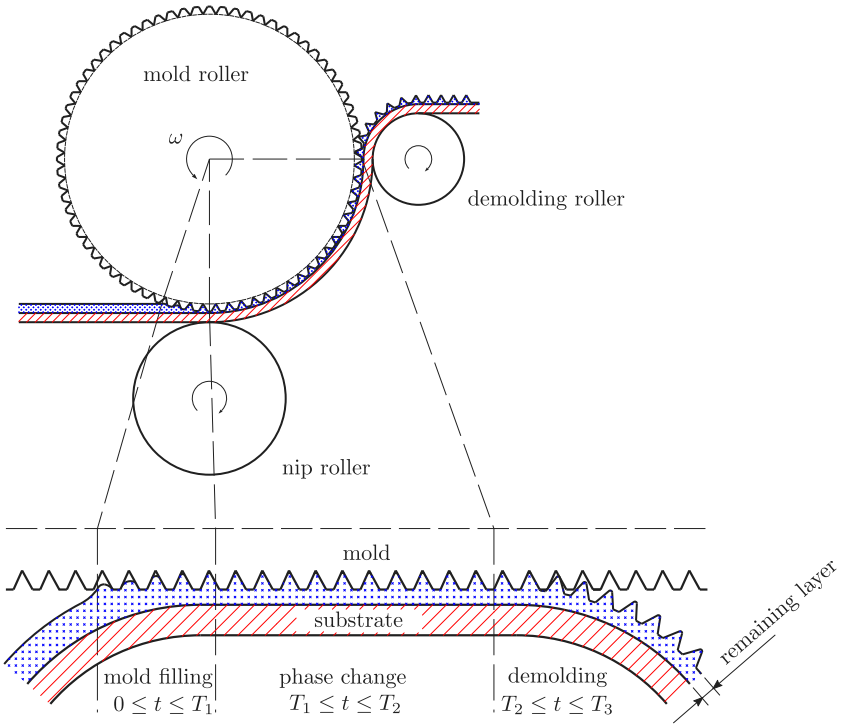

Fig. 1. Illustration of the R2RNIL sub-processes (mold filling, phase change, and demolding) and the regions of the mold roller and time intervals for each sub-process. In mold filling, the stress-free fluid film on the substrate flows into the mold pattern cavities, which is followed by the phase change sub-process in which the substrate is irradiated with UV light to cure the coated film in the pattern. A demolding roller is employed to peel-off the patterned substrate from the mold roller and the substrate is transported downstream.

Rajagopal, 2008, Moon, Cui, & Rao, 2015, Sodhi, Cruz, & Rao, 2015). These studies share much in common with our study where the phase change is affected by ultraviolet radiation, but there is no "shape memory" that needs to be taken into consideration. Recently, Sreejith, Kannan, and Rajagopal (2021) studied the warpage and shrinkage and the resultant residual stresses that arise in amorphous polymers during phase change in the process of additive manufacturing, using the identical thermodynamic framework. Suffice it is to say that all the above-mentioned studies share the same thermodynamic basis with the study being carried out here.

In Gomez-Constante, Pagilla, and Rajagopal (2019, 2020) we discussed some previous models describing roll-to-roll Nanoimprinting Lithography (Ahn & Guo, 2009; Jain & Bonnecaze, 2013; Kim, Kim, & Sin, 2009; Lin & Chen, 2008; Wang, Li, Qiu, & Zhou, 2018; Young, 2005) and some experimental results (Ahn et al., 2013; Inanami, Ojima, Matsuki, Kono, & Nakasugi, 2012; Lee, Kim, Kwak, & Suh, 2009; Mäkelä, Haatainen, & Ahopelto, 2011; Matschuk & Larsen, 2012; Sohn, Park, Lee, Jang, & Lee, 2013; Thesen, Nees, et al., 2014; Thesen et al., 2014; Wu, Sung, Yao, & Chen, 2013) obtained in the search for higher throughput and better geometric tolerances. We also identified the sub-processes that are always present in the same order but with slight differences depending on the specific purpose for a given application, namely *mold filling*, *phase change* and *demolding* (Fig. 1). In this paper we will develop a model for the phase change process by considering how photo-chemical reactions affect the change of phase from a viscoelastic fluid into a viscoelastic solid (see Kannan & Rajagopal, 2004) and the different boundary and initial conditions; the model development will be based on the thermomechanical framework in Rajagopal and Srinivasa (2000) and Rao and Rajagopal (2002) and its generalization to take into account chemical reactions (Kannan & Rajagopal, 2011). We focus on the characteristics that both the stored energy and the rate of dissipation functions must have in order to simulate how crystallization occurs in polymers by taking into account the interaction of both constituents within the context of the Mechanics of Mixtures (see Atkin & Craine, 1976; Bowen, 1967; Rajagopal & Tao, 1995; Truesdell, 1962). In particular, we take into account how the intensity of UV light affects the evolution of the mass fraction of melt and solid portions of the mixture (Chandrasekhar, 2013). The formulation proposed for phase change in this work can describe the most common curing processes, including those that involve thermal and photo-chemical reactions.

Assuming that we start with a nano-scaled mold feature completely filled with a viscoelastic fluid, that no external forces other than the tension of the web are acting on the system, and that the only external source of energy is the UV light source irradiating the substrate, the model will provide the evolution of the viscoelastic fluid film inside the mold cavity as it is converted into a viscoelastic solid and how the internal stresses on the mixture are affected. Non-inertial forces resulting from the relative circular motion across the mold roller will also be taken into account in the formulation.

We start by determining the form of the Cauchy stress tensors for both the viscoelastic fluid and viscoelastic solid constituents of the mixture that maximizes the rate of entropy production. Next, we determine the amount of fluid converted into solid by

irradiating it with UV light, which along with the conservation laws results in a model consisting of a well-posed system of partial differential equations. The corresponding initial conditions are determined by the final conditions of the linearized mold filling problem (Gomez-Constante et al., 2019, 2020). The boundary conditions are determined by the interaction of the mixture with both the tension of the web and the UV light source.

The organization of the paper is as follows. In Section 2, we derive the constitutive equations of the constituents of the mixture based on the maximization of the rate of entropy production. Section 3 deals with the photo-chemistry of Photo-tunable Molecular Crosslinking (PMC) and the Radiative Transfer Function. In Section 4, we derive the initial and boundary conditions by taking into account the information about the final state of the previous mold filling process. Section 5 provides the general nonlinear system of equations for the phase change process and in Section 6 we obtain a quasi-linearized version of the nonlinear model that enables a numerical approximation that still exhibits the qualitative behavior that we conjecture is adequate for phase change. Section 7 is concerned with numerical simulations of the process depicting the more important qualitative behavior of the model. Conclusions and future directions are provided in Section 8.

2. Thermodynamic framework for the constitutive equations

We will develop a model that considers the general theory of the mechanics of mixtures (Rajagopal & Tao, 1995) along with the assumption that the rate of dissipation function due to mechanical working on each constituent is maximized. We will find the constitutive equations that both constituents of the mixture must have in order to satisfy the conservation laws.

2.1. Kinematics of motion of a mixture

Let us consider a mixture of two constituents: a viscoelastic fluid (or melt) and a viscoelastic solid. We shall denote with subscripts m and s the melt and solid constituents, respectively. Let $\mathbf{X}_i$ $(i = m, s)$ be a material point belonging to constituent i in the reference state. The motion of each constituent is defined through

$$\begin{aligned}\chi_i &: \kappa_R(\mathcal{B}) \times \mathbb{R}^+ \longrightarrow \kappa_t(\mathcal{B}),\\ &(\mathbf{X}_i, t) \longmapsto \chi_i(\mathbf{X}_i, t) =: \mathbf{x}.\end{aligned}$$

Assuming the motion to be adequately smooth, the deformation gradients ($\boldsymbol{F}_i$) and the left and right Cauchy–Green tensors ($\boldsymbol{B}_i$ and $\boldsymbol{C}_i$) are given by

$$\boldsymbol{F}_i \overset{\text{def}}{=} \frac{\partial \chi_i}{\partial \mathbf{X}_i}, \quad \boldsymbol{B}_i \overset{\text{def}}{=} \boldsymbol{F}_i \boldsymbol{F}_i^T, \quad \boldsymbol{C}_i \overset{\text{def}}{=} \boldsymbol{F}_i^T \boldsymbol{F}_i. \tag{1}$$

Assuming there is no relative motion between the constituents of the mixture, i.e.,

$$\boldsymbol{v} = \frac{\partial \chi_m}{\partial t} = \frac{\partial \chi_s}{\partial t}, \tag{2}$$

the velocity gradient of the constituents is given by

$$\boldsymbol{L}_i = \text{grad } \boldsymbol{v}. \tag{3}$$

In addition, if we assume and that the temperature of the mixture (θ) is the same for each constituent, i.e.,

$$\theta_i = \theta \tag{4}$$

and both constituents coexist at the same material points, then by additivity of mass, the density of the mixture (ρ) satisfies

$$\rho = \rho_m + \rho_s. \tag{5}$$

Now, the conservation of mass for each constituent of the mixture is given by

$$\frac{d\rho_i}{dt} + \rho_i \text{ div } \boldsymbol{v} = m_i \tag{6}$$

where m_i is the mass production rate of each constituent i. Since the mass fraction of melt changing phase into solid must be equal to the mass fraction of solid created, they must satisfy

$$m_m + m_s = 0. \tag{7}$$

Substituting Eq. (6) into Eq. (7) we obtain the conservation of mass of the mixture as

$$\frac{d\rho}{dt} + \rho \text{ div } \boldsymbol{v} = 0. \tag{8}$$

The angular momentum supply is asumed to be zero and the Cauchy stress associated with the constituents are assumed to be symmetric. Using a similar reasoning and assuming that each constituent satisfies the conservation of linear momentum, we get that the conservation of linear momentum for each constituent and the mixture to be given by

$$\rho_i \frac{d\boldsymbol{v}}{dt} = \text{div } \boldsymbol{T}_i + \rho_i \boldsymbol{b}_i + \boldsymbol{m}_i \tag{9}$$

$$\rho \frac{d\boldsymbol{v}}{dt} = \text{div } \boldsymbol{T} + \rho \boldsymbol{b} \tag{10}$$

where $\boldsymbol{T}_i$ and $\boldsymbol{b}_i$, respectively, are the Cauchy stress tensor and body force of constituent i, and $\boldsymbol{m}_i$ is the momentum generated by mass production of constituent i which satisfies

$$\boldsymbol{m}_m + \boldsymbol{m}_s = \boldsymbol{0}. \tag{11}$$

The Cauchy stress tensor ($\boldsymbol{T}$) and the body force ($\boldsymbol{b}$) acting on the mixture are given by

$$\boldsymbol{T} = \boldsymbol{T}_m + \boldsymbol{T}_s, \tag{12}$$

$$\rho \boldsymbol{b} = \rho_m \boldsymbol{b}_m + \rho_s \boldsymbol{b}_s. \tag{13}$$

The conservation of energy for each constituent and the mixture are given by

$$\rho_i \frac{d\epsilon_i}{dt} = -\text{div } \boldsymbol{q}_i + \boldsymbol{T}_i \cdot \boldsymbol{L} + \rho_i r_i + \epsilon_i^s \tag{14}$$

$$\rho \frac{d\epsilon}{dt} = -\text{div } \boldsymbol{q} + \boldsymbol{T} \cdot \boldsymbol{L} + \rho r \tag{15}$$

where the heat flux ($\boldsymbol{q}$), internal energy ($\rho\epsilon$) and radiant heating of the mixture (ρr) are defined as

$$\boldsymbol{q} = \boldsymbol{q}_m + \boldsymbol{q}_s, \tag{16}$$

$$\rho\epsilon = \rho_m \epsilon_m + \rho_s \epsilon_s, \tag{17}$$

$$\rho r = \rho_m r_m + \rho_s r_s. \tag{18}$$

The energy supply (ϵ_i^s) of both constituents satisfy

$$\epsilon_m^s + m_m \epsilon_m + \epsilon_s^s + m_s \epsilon_s = 0. \tag{19}$$

Finally, by defining the Helmholtz potential function (ψ) and the entropy (s) of the mixture as

$$\rho\psi = \rho_m \psi_m + \rho_s \psi_s, \tag{20}$$

$$\rho s = \rho_m s_m + \rho_s s_s, \tag{21}$$

we find the reduced energy-dissipation equation of the constituents and the mixture as

$$\boldsymbol{T}_i \cdot \boldsymbol{L} - \rho \frac{d}{dt}\left(\frac{\rho_i \psi_i}{\rho}\right) - \rho_i s_i \frac{d\theta}{dt} + \epsilon_i^s + m_i \epsilon_i - \frac{1}{\theta} \boldsymbol{q}_i \cdot \text{ grad } \theta \geq 0 \tag{22}$$

$$\boldsymbol{T} \cdot \boldsymbol{L} - \rho \frac{d\psi}{dt} - \rho s \frac{d\theta}{dt} - \frac{1}{\theta} \boldsymbol{q} \cdot \text{grad } \theta \geq 0. \tag{23}$$

By defining the mass fraction of the melt as

$$\alpha = \frac{\rho_m}{\rho}, \tag{24}$$

where $0 \leq \alpha(\boldsymbol{x}, t) \leq 1$, we can now see that the body force, internal energy, radiant heating, Helmholtz potential and entropy of the mixture are defined as a convex combination of the mass fraction of both the melt and the solid. In addition, we have

$$\frac{d\psi}{dt} = \frac{d}{dt}\left[\alpha\psi_m + (1-\alpha)\psi_s\right] = \alpha \frac{d\psi_m}{dt} + (1-\alpha)\frac{d\psi_s}{dt} + (\psi_m - \psi_s)\frac{d\alpha}{dt}. \tag{25}$$

Substituting Eq. (25) into Eq. (23) and comparing it with the sum of the individual constituents defined by Eq. (22), we have

$$-\rho(\psi_m - \psi_s)\frac{d\alpha}{dt} = -m_m \psi_m - m_s \psi_s. \tag{26}$$

From Eqs. (7) and (26), we have

$$\rho \frac{d\alpha}{dt} = m_m, \tag{27}$$

which basically states that the change in the mass fraction of the melt is proportional to its mass production rate per unit volume. By using the conservation of mass and the definition of Helmholtz potential of each constituent, we obtain

$$-\rho \frac{d}{dt}\left(\frac{\rho_i \psi_i}{\rho}\right) + m_i \epsilon_i = -\rho_i \frac{d\psi_i}{dt} + m_i \theta s_i \tag{28}$$

Substituting Eq. (28) into Eq. (22) yields

$$\boldsymbol{T}_i \cdot \boldsymbol{L} - \rho_i \frac{d\psi_i}{dt} - \rho_i s_i \frac{d\theta}{dt} + \epsilon_i^s + m_i \theta s_i - \frac{1}{\theta} \boldsymbol{q}_i \cdot \text{grad } \theta \geq 0. \tag{29}$$

We next define

$$\zeta_i = \boldsymbol{T}_i \cdot \boldsymbol{L} - \rho_i \frac{d\psi_i}{dt} - \rho_i s_i \frac{d\theta}{dt} \tag{30}$$

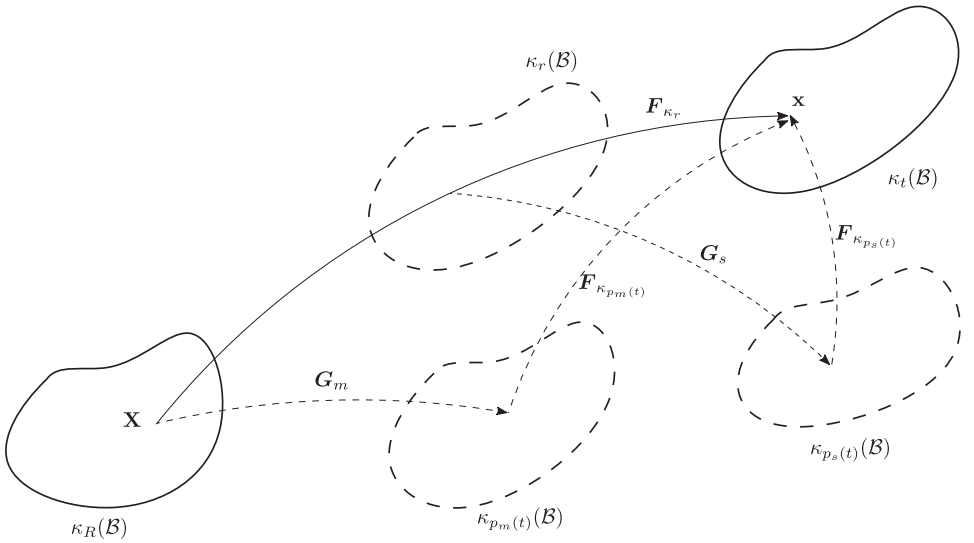

Fig. 2. Illustrations of the evolving configurations of the body $\mathcal{B}$: the reference configurations for the melt and solid (that occurs when phase change starts), natural configurations for melt and solid (denoted with their respective sub-indexes) and current configurations of the body denoted as $\kappa_R(\mathcal{B})$, $\kappa_r(\mathcal{B})$, $\kappa_{p_m(t)}(\mathcal{B})$, $\kappa_{p_s(t)}(\mathcal{B})$ and $\kappa_t(\mathcal{B})$, respectively, with deformation gradient $\boldsymbol{F}_{\kappa_R}$ and mappings $\boldsymbol{G}_m$, $\boldsymbol{G}_s$, $\boldsymbol{F}_{\kappa_{p_m(t)}}$, $\boldsymbol{F}_{\kappa_{p_s(t)}}$ shown.

$$\zeta_i^p = \epsilon_i^s + m_i \theta s_i \tag{31}$$

$$\zeta_i^c = -\frac{1}{\theta}\boldsymbol{q}_i \cdot \operatorname{grad}\,\theta \tag{32}$$

where ζ_i, ζ_i^p and ζ_i^c are the rate of entropy production due to mechanical working, phase change and heat conduction, respectively. We will assume that they are all non-negative scalar functions. In order to find the appropriate constitutive equations for our mixture, we will use a thermomechanical approach consisting of the maximization of the rate of entropy production of mechanical working of the mixture defined as

$$\zeta = \zeta_m + \zeta_s \tag{33}$$

along with the restriction of isochoric motion enforced on the natural configurations explained below.

For what comes next, we assume that both the melt and solid constituents of the mixture have natural configurations $\kappa_{p_m(t)}$ and $\kappa_{p_s(t)}$, respectively (Fig. 2). Using these natural configurations, we can now define the mappings from their respective reference configurations (for the melt and the solid) as

$$\boldsymbol{G}_m = \boldsymbol{F}_{\kappa_R \to \kappa_{p_m(t)}} \overset{\text{def}}{=} \boldsymbol{F}^{-1}_{\kappa_{p_m(t)}} \boldsymbol{F} \tag{34}$$

$$\boldsymbol{G}_s = \boldsymbol{F}_{\kappa_r \to \kappa_{p_s(t)}} \overset{\text{def}}{=} \boldsymbol{F}^{-1}_{\kappa_{p_s(t)}} \boldsymbol{F}_{\kappa_r}. \tag{35}$$

where the tensors associated with the natural configurations for the melt and the solid are $\boldsymbol{F}_{\kappa_{p_m(t)}}$ and $\boldsymbol{F}_{\kappa_{p_s(t)}}$ respectively. Now, we proceed to define the velocity gradient and the mappings associated with both natural configurations as

$$\boldsymbol{L}_{\kappa_{p_i(t)}} \overset{\text{def}}{=} \dot{\boldsymbol{G}}_i \boldsymbol{G}_i^{-1} \tag{36}$$

which then allows us to define their symmetric parts as

$$\boldsymbol{D}_i = \frac{1}{2}\left(\boldsymbol{L}_{\kappa_{p_i(t)}} + \boldsymbol{L}^T_{\kappa_{p_i(t)}}\right) \tag{37}$$

$$\boldsymbol{D} = \frac{1}{2}\left(\boldsymbol{L} + \boldsymbol{L}^T\right). \tag{38}$$

For the sake of simplicity, we assume that the Helmholtz potential ψ_m and the rate of entropy production ζ_m of the melt are given by

$$\psi_m(\theta, \boldsymbol{B}_{\kappa_{p_m(t)}}) = \frac{G_m \theta}{2\rho_{0_m}\theta_0} \operatorname{tr}\, \boldsymbol{B}_{\kappa_{p_m(t)}} \tag{39}$$

$$\zeta_m(\theta, \boldsymbol{B}_{\kappa_{p_m(t)}}, \boldsymbol{D}_{\kappa_{p_m(t)}}) = 2\mu_m \boldsymbol{D}_{\kappa_{p_m(t)}} \cdot \boldsymbol{B}_{\kappa_{p_m(t)}} \boldsymbol{D}_{\kappa_{p_m(t)}} \tag{40}$$

and the Helmholtz potential ψ_s and the rate of entropy production ζ_s of the solid by

$$\psi_s(\theta, \boldsymbol{B}_{\kappa_{p_s(t)}}) = \frac{G_{1s}}{2\rho_{0_s}}(\operatorname{tr}\, \boldsymbol{B}_{\kappa_{p_s(t)}} - 3) + \frac{G_{2s}}{2\rho_{0_s}}(\operatorname{tr}\, \boldsymbol{B}_{\kappa_r} - 3) \tag{41}$$

$$\zeta_s(\theta, \boldsymbol{B}_{\kappa_{p_s(t)}}, \boldsymbol{D}_{\kappa_{p_s(t)}}) = 2\mu_s \boldsymbol{D}_{\kappa_{p_s(t)}} \cdot \boldsymbol{B}_{\kappa_{p_s(t)}} \boldsymbol{D}_{\kappa_{p_s(t)}}. \tag{42}$$

where ρ_{0_i} is the initial density of the constituent and G_i, μ_i are material coefficients related to each constituent and θ_0 is the initial temperature of the mixture.

Maximizing the rate of entropy production (Eq. (33)) along with the restrictions of both natural configurations associated with each of the constituents being isochoric, we have

$$\text{tr } \boldsymbol{D}_{\kappa_{p_i(t)}} = 0 \tag{43}$$

Further, the Cauchy stress tensor of the melt $\boldsymbol{T}_m$ is given by

$$\boldsymbol{T}_m = \rho_m \frac{G_m \theta}{\rho_{0_m} \theta_0} \boldsymbol{B}_{\kappa_{p_m(t)}} \tag{44}$$

$$\mu_m \overset{\nabla}{\boldsymbol{B}}_{\kappa_{p_m(t)}} = \rho_m \frac{G_m \theta}{\rho_{0_m} \theta_0} \left(\frac{3}{\text{tr } \boldsymbol{B}^{-1}_{\kappa_{p_m(t)}}} \boldsymbol{I} - \boldsymbol{B}_{\kappa_{p_m(t)}} \right) \tag{45}$$

and the Cauchy stress tensor of the solid $\boldsymbol{T}_s$ is given by

$$\boldsymbol{T}_s = \rho_s \frac{G_{1s}}{\rho_{0_s}} \boldsymbol{B}_{\kappa_{p_s(t)}} + \rho_s \frac{G_{2s}}{\rho_{0_s}} \boldsymbol{B}_{\kappa_r} \tag{46}$$

$$\mu_s \overset{\nabla}{\boldsymbol{B}}_{\kappa_{p_s(t)}} = \rho_s \frac{G_{1s}}{\rho_{0_s}} \left(\frac{3}{\text{tr } \boldsymbol{B}^{-1}_{\kappa_{p_s(t)}}} \boldsymbol{I} - \boldsymbol{B}_{\kappa_{p_s(t)}} \right) \tag{47}$$

where $\overset{\nabla}{\boldsymbol{B}}$ is the upper-convected time derivative defined as

$$\overset{\nabla}{\boldsymbol{B}} = \dot{\boldsymbol{B}} - \boldsymbol{L}\boldsymbol{B} - \boldsymbol{B}\boldsymbol{L}^T. \tag{48}$$

Rearranging terms and considering that $\overset{\nabla}{\boldsymbol{B}}_{\kappa_r} = \boldsymbol{0}$, the constitutive equations of the melt and solid are given by

$$\boldsymbol{T}_m = \frac{\rho_m}{\rho_{0_m}} \frac{G_m \theta}{\theta_0} \boldsymbol{I} + \frac{\rho_m}{\rho_{0_m}} \boldsymbol{S}_m \tag{49}$$

$$\frac{\mu_m}{G_m} \left(\frac{\theta_0}{\theta} \right) \overset{\nabla}{\boldsymbol{S}}_m + \left[\frac{\rho_m}{\rho_{0_m}} + \frac{\mu_m}{G_m} \frac{d}{dt} \left(\frac{\theta_0}{\theta} \right) \right] \boldsymbol{S}_m = \frac{\rho_m}{\rho_{0_m}} \frac{G_m \theta}{\theta_0} \left(\frac{3}{\text{tr } \boldsymbol{B}^{-1}_{\kappa_{p_m(t)}}} - 1 \right) \boldsymbol{I} + 2\mu_m \boldsymbol{D} \tag{50}$$

and

$$\boldsymbol{T}_s = \frac{\rho_s}{\rho_{0_s}} \boldsymbol{S}_s \tag{51}$$

$$\frac{\mu_s}{G_{1s}} \overset{\nabla}{\boldsymbol{S}}_s + \frac{\rho_s}{\rho_{0_s}} \boldsymbol{S}_s = \frac{\rho_s}{\rho_{0_s}} G_{1s} \left(\frac{3}{\text{tr } \boldsymbol{B}^{-1}_{\kappa_{p_s(t)}}} \boldsymbol{I} + \frac{G_{2s}}{G_{1s}} \boldsymbol{B}_{\kappa_r} \right) \tag{52}$$

Note that the constitutive equations describe the behavior of the melt and solid constituents of the mixture independently. However, this formulation does not explain how the densities of the constituents evolve in time due to UV light irradiation; to describe this we need the governing equations for the photochemistry of the phase change of the mixture which we describe below.

3. Photochemistry of phase change using UV light

Photochemical reactions are a special class of chemical reactions that are activated by irradiation of light of certain energy determined by their frequency. Photons of certain frequency (in the ultraviolet electromagnetic spectrum in our case) are the ones that trigger the chemical reaction by adding energy to the molecules and interacting with the valence electrons of the molecules composing the polymeric chains used for this manufacturing process.

Generally speaking, there are two main types of photo-chemical reactions: Photo-Induced Network Rearrangement (PNR) are chemical reactions in which the initial molecular chain is broken by the irradiation of UV light, producing two smaller molecules one of which is the one that possesses the desired mechanical properties; and Photo-tunable Molecular Crosslinking (PMC) which is an internal reconfiguration of certain parts of the chain of the polymer that are triggered by the irradiation of UV light and produces the stiffening of these long chains, macroscopically producing the desired mechanical properties. PNR reactions need additional stoichiometric balance equations along with some extra terms that will appear in the reduced energy-dissipation equation (Eq. (22)) making this approach more complicated, whereas for PMC reactions all we need is an experimentally determined equation relating the amount of polymeric fluid being converted from one phase into the other in terms of time. Both PNR and PMC reactions are governed by the same physical principle that governs the interaction between matter and electromagnetic radiations.

3.1. Radiative transfer equation

Let us suppose that we have an electromagnetic radiation field emitted by a source that passes through a medium. The amount of energy in the form of radiation that is absorbed by the medium, transmitted through the medium, and scattered in different directions across the medium is governed by the equation (Chandrasekhar, 2013)

$$\frac{1}{c}\frac{\partial I}{\partial t} + \hat{r}\cdot\frac{\partial I}{\partial \mathbf{x}} + (\sigma_s + a_m c_m + a_s c_s)I = j_\nu + \frac{c}{4\pi}\sigma_s \int_\Gamma I_\nu da \tag{53}$$

where c is the speed of light, I is the intensity of the light through the medium, σ_s is the absorbance due to the scattering, a_m is the absorption coefficient of the melt, c_m is the molar concentration per volume of the melt, a_s is the absorption coefficient of the solid, c_s is the molar concentration per volume of the solid, j_ν is the radiation emitted by the medium and I_ν is the scattering kernel that takes into account the non-homogeneous nature of the medium. Since we are not dealing with radioactive materials and the scale of the process is very small, it is reasonable to neglect scattering and emission, which reduces the equation to:

$$\frac{1}{c}\frac{\partial I}{\partial t} + \hat{r}\cdot\frac{\partial I}{\partial \mathbf{x}} + (a_m c_m + a_s c_s)I = 0 \tag{54}$$

where $\hat{r}$ is the unit radial vector along the direction in which light propagates inside the medium. Notice that if we neglect the time derivative in the previous equation then we recover the well known Beer–Lambert Equation.

3.2. Photochemistry of PMC processes

Conservation laws alone cannot describe the response of bodies, one needs constitutive specifications, similarly the radiative transfer equation alone is not enough to describe photo-chemical reactions. Additional equations describing the particular behavior of the molecular chains forming the materials in the mixture is needed. The process for obtaining such equations is out of the scope of our work, so we will just use a rather simple specification. We will assume that the variation in time of the molar concentration of the melt is given by the equation

$$\frac{\partial c_m}{\partial t} = -\frac{\epsilon_m}{N_A h\nu} c_m^2 I \tag{55}$$

where $N_A = 6.022\times 10^{23}\ \text{mol}^{-1}$ is the Avogadro's constant, $h = 6.626\times 10^{-34}\ \text{J}\cdot\text{s}$ is the Planck's constant, ν is the frequency of the photon and c_0 is the concentration of the mixture at the beginning of the process. In this particular case, we have assumed that the photo-chemical reaction is bi-molecular which is why the exponent of the molar concentration is equal to 2 (Long, Scott, Qi, Bowman, & Dunn, 2009). In addition, the molar concentration per volume of a chemical component i is related to density via

$$\rho_i = c_i M_i \tag{56}$$

where ρ_i is the density of constituent i and M_i is its corresponding molecular weight. With this relation between the density and molar concentration per unit volume for each constituent, we can now express how the densities of both constituents will evolve in time in terms of the thermomechanical and the photochemical behavior.

4. Boundary conditions for phase change problem

Let us assume a system consisting of three parallel rigid rollers: a mold roller of outer radius R_o rotating at constant angular speed ω, a nip roller producing the filling of the cavities imprinted in the mold roller and an auxiliary demolding roller. The separation between the secondary rollers produce a fixed wrapping angle which for the sake of simplicity we will set as $\varphi = \pi/2$ thus determining the arc which is the zone where phase change will take place (Fig. 3).

In addition, we will assume that mold filling has successfully been accomplished in the previous sub process meaning that the mold cavity has been filled with fluid up to a given minimum accepted tolerance.

Since the angular speed is assumed to be constant, the available time for changing phase from a viscoelastic fluid to a viscoelastic solid denoted as $T_2 - T_1$ is given by

$$T_2 - T_1 = \frac{\varphi}{\omega}. \tag{57}$$

For phase change, the boundary condition is given in terms of the normal reaction that balances the tension of the web that acts as a traction force on the substrate. To elaborate, let us consider a small portion of the substrate φ (Fig. 4).

To simplify things a little bit, it suffices to assume that the tension of the web $\vec{t}_w$ is uniform across the substrate thickness and in the tangential direction. This tension along with the curvature of the roller produces a reaction force in the normal (radial) direction which keeps the fluid inside the mold cavity from being expelled by both the non inertial forces and the energy stored from the previous mold filling sub process. Therefore, the boundary condition at the substrate is

$$\rho \boldsymbol{v}(\boldsymbol{v}\cdot\hat{n}) = (\boldsymbol{T} - \boldsymbol{T}_{subs})\hat{n} \tag{58}$$

where $\boldsymbol{T}_{subs}$, $\boldsymbol{T}$ are the Cauchy stress tensors in the substrate and the melt respectively and $\hat{n}$ is the unit outward pointing normal in the substrate direction.

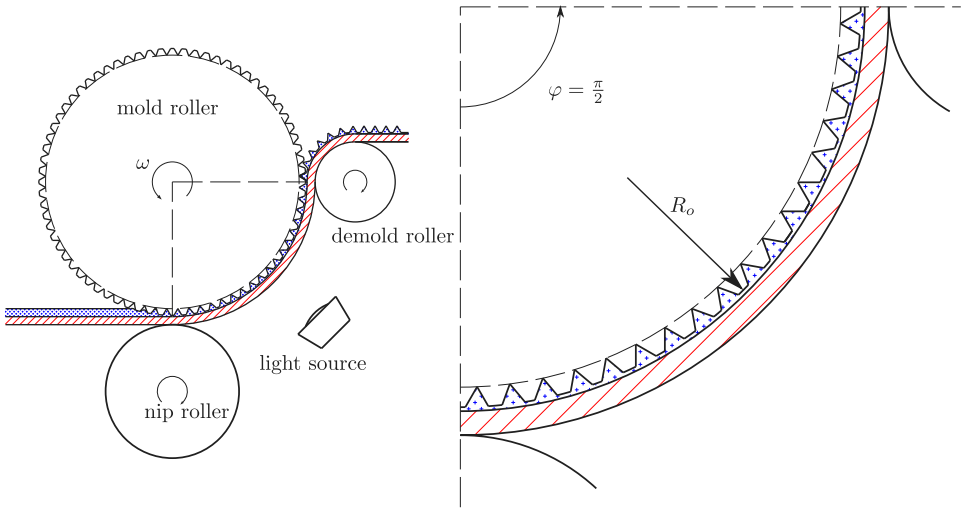

Fig. 3. Kinematics of R2RNIL phase change.

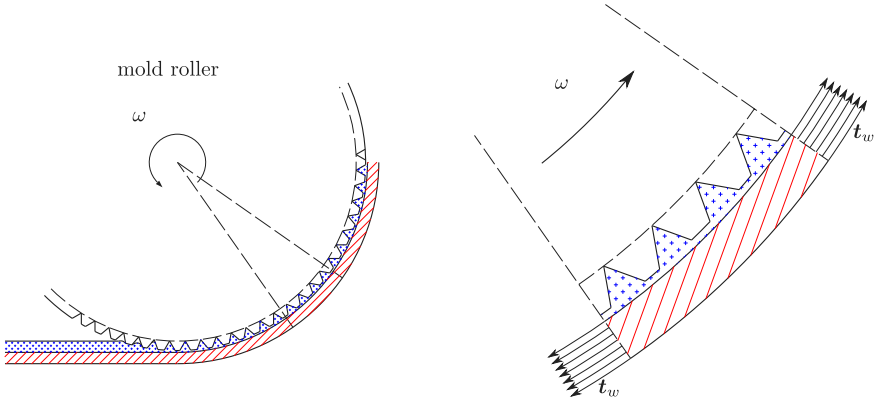

Fig. 4. Web forces for a small portion of substrate.

4.1. Heat transfer

Since the mold patterns and the fluid film are in the nano-scale, most of the energy irradiated from the UV light source will not be absorbed by the fluid. In fact, we expect that the vast majority of that energy will be absorbed by the mold roller and reflected back to the surroundings making this a possibly temperature-dependent process. We identified two main interactions between the fluid film and its surroundings: heat conduction between the fluid and the mold and heat convection between the fluid and the air trapped inside the mold cavity (Fig. 5).

Assuming the manufacturing process runs at constant parameters, the interaction between the fluid and the mold can be modeled as a constant heat flux $\vec{q}_{mold}$ that flows from the mold roller into the fluid, increasing the temperature of the fluid

$$-k(\text{grad}\ \theta) = \vec{q}_{\text{mold}} \tag{59}$$

where k is the conductivity of the fluid. For the interaction in between the fluid and the air we can assume that convection of the fluid is given by

$$-k(\text{grad}\ \theta)\cdot\hat{n} = h_c A(\theta - \theta_{\text{air}}) \tag{60}$$

where h_c is the heat transfer coefficient and A is the area of the free surface. The latter applies to the interaction between fluid and substrate because of the lumped heat capacity assumption.

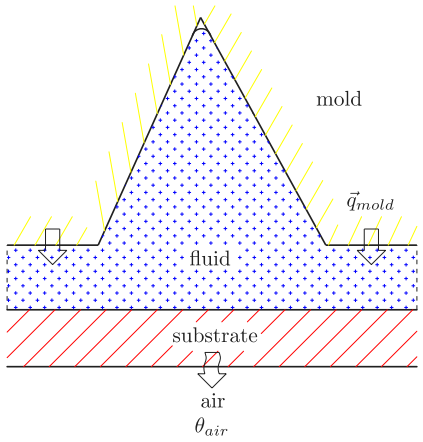

Fig. 5. Thermal interaction of the fluid film with the surroundings.

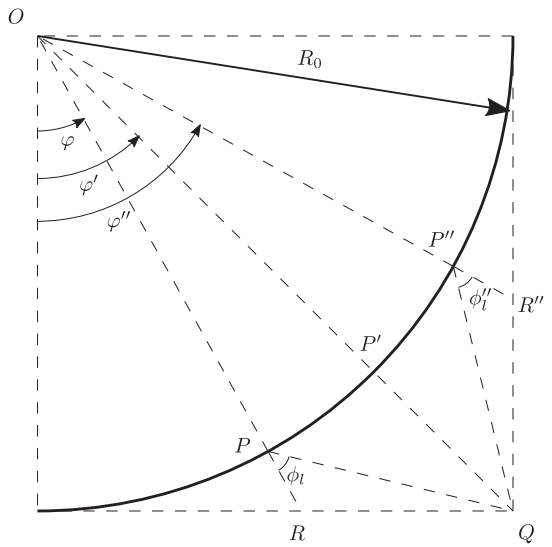

Fig. 6. Angle of incidence of UV light and how it changes over the trajectory $0 \leq \varphi \leq \frac{\pi}{2}$.

4.2. Photo-chemistry of phase change

Similar to what happens with rays of sunlight irradiating our planet at human-scale structures, the nano-scale of the features makes it possible to assume that UV light rays irradiating each mold feature are parallel and that only their direction (which is now uniform) will change with time.

For the sake of simplicity, we will assume that the source of UV light is located at a point fixed in space, say Q, such that it irradiates a total angle of $\pi/2$ rad (Fig. 6). This has been done with the purpose of avoiding multiple light sources and all the modeling complications arising from such an assumption. Let us think of a fixed material point in the mixture denoted by P. As it travels across the arc of length $\frac{\pi}{2}R_0$, the light rays form an angle ϕ_l between the normal to the surface at point P and the straight line joining point P and the position of the light source Q. At position $\theta = \frac{\pi}{4}$ the triangle formed by points P, Q and R degenerates into a straight line to then reverse its direction. With all these considerations, the angle formed between the normal direction at point P and the UV-light ray is governed by the equation

$$\sin\phi_l = \frac{|\cos\varphi - \sin\varphi|}{\sqrt{(1-\sin\varphi)^2 + (1-\cos\varphi)^2}}. \tag{61}$$

Now, let us consider what happens with the mixture inside one feature. First, the Law of Refraction (also known as Snell's Law) states that the angle of refraction depends on the medium in which light travels, and that between two adjacent media with flat

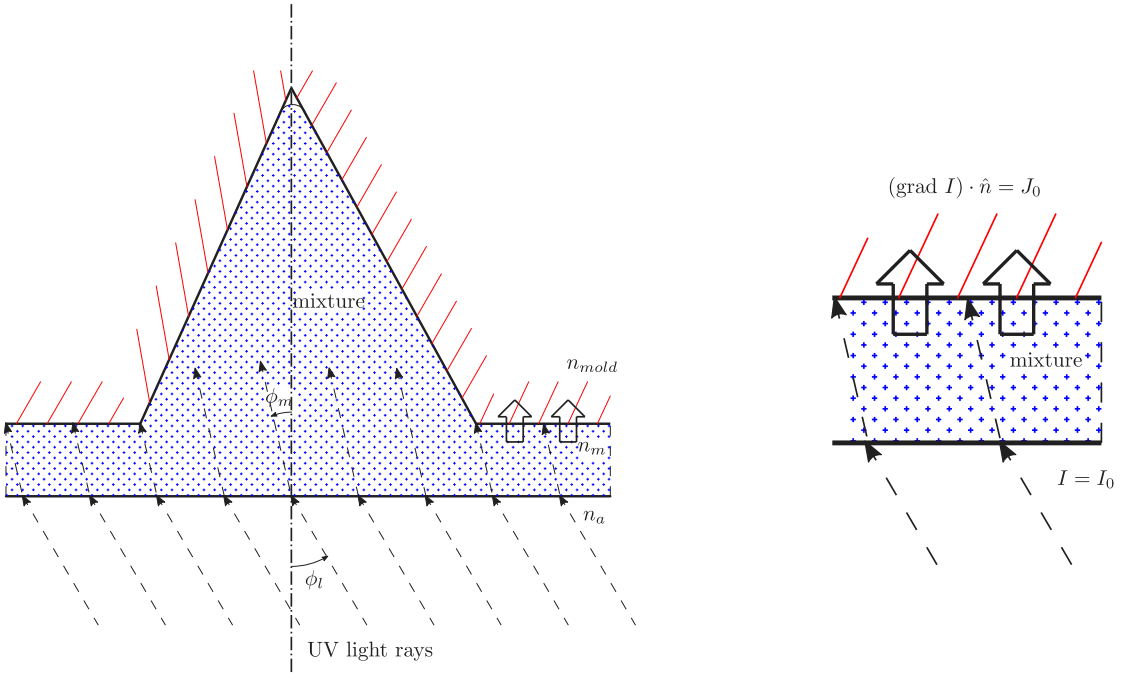

Fig. 7. Angle of incidence of UV light for a single mold feature (left). It clearly shows how the angle of incidence changes from ϕ_l when light travels through air to ϕ_m when it travels through the mixture. Boundary conditions of the intensity of light I at the boundaries (right).

boundary (Fig. 7) it is governed by equation

$$\frac{\sin \phi_l}{\sin \phi_m} = \frac{n_m}{n_a} \tag{62}$$

where ϕ_l is the angle at which light travels through air, ϕ_m is the angle at which light travels through the mixture, n_a is the refraction index for air and n_m is the refraction index for the mixture. In order to simplify the analysis, we will not take into account the light that will be reflected in the mixture/mold-roller interface which will provide some additional energy for the phase change process.

With all the previous considerations, we can finally determine the direction $\hat{r}$ (in the radiative transfer function (Eq. (54))) at which light travels inside the mixture as

$$\hat{r} = -\sin \phi_m \hat{e}'_\theta + \cos \phi_m \hat{e}'_r \tag{63}$$

where $\hat{e}'_\theta$ is the tangential direction along the motion (horizontal), $\hat{e}'_r$ is the radial direction (vertical) and $\sin \phi_m$ and $\cos \phi_m$ are given by the equations

$$\sin \phi_m = \frac{n_a}{n_m} \sin \phi_l \tag{64}$$

$$\cos \phi_m = \sqrt{1 - \left(\frac{n_a}{n_m} \sin \phi_l \right)^2} \tag{65}$$

As for the boundary conditions, we will assume that the intensity of the light that reaches the outer surface of the mixture remains constant throughout the whole phase change process (which is not true since the curvature of the roller and the absorption of air will affect the intensity that reaches the outer boundary at each position across the arc), whereas the in the interface between the mixture and the mold roller we assume a constant light intensity flux which depends on the light intensity at that boundary, both expressed as:

$$I = I_0 \tag{66}$$

$$(\text{grad } I) \cdot \hat{n} = J_0 \tag{67}$$

respectively. These boundary conditions along with the symmetric assumptions on the left and right boundaries of the feature makes the problem well-posed in terms of number of equations and unknowns.

5. Governing equations for general formulation of phase change

From all the previous analysis and simplifications, we can now state that the governing equations that define phase change of the mixture:

$$\rho \frac{d\boldsymbol{v}}{dt} = \text{div } \boldsymbol{T} \tag{68}$$

$$\frac{d\rho}{dt} + \rho \text{ div } \boldsymbol{v} = 0 \tag{69}$$

$$\rho \frac{d\epsilon}{dt} = \boldsymbol{T} \cdot \boldsymbol{D} + \text{div}(k \text{ grad } \theta) \tag{70}$$

$$\frac{1}{c}\frac{\partial I}{\partial t} + \hat{r} \cdot \frac{\partial I}{\partial \mathbf{x}} + (a_m c_m + a_s c_s) I = 0 \tag{71}$$

$$\boldsymbol{T} = -p\boldsymbol{I} + \boldsymbol{T}_m + \boldsymbol{T}_s \tag{72}$$

$$\rho = \rho_m + \rho_s \tag{73}$$

$$\rho_i = c_i M_i \tag{74}$$

along with the constitutive equations and experimentally determined photochemical behavior defined by

$$\boldsymbol{T}_m = \frac{\rho_m}{\rho_{0_m}} \frac{G_m \theta}{\theta_0} \boldsymbol{I} + \frac{\rho_m}{\rho_{0_m}} \boldsymbol{S}_m \tag{75}$$

$$\boldsymbol{T}_s = \frac{\rho_s}{\rho_{0_s}} \boldsymbol{S}_s \tag{76}$$

$$\frac{\mu_m}{G_m}\left(\frac{\theta_0}{\theta}\right) \overset{\nabla}{\boldsymbol{S}}_m + \left[\frac{\rho_m}{\rho_{0_m}} + \frac{\mu_m}{G_m}\frac{d}{dt}\left(\frac{\theta_0}{\theta}\right)\right] \boldsymbol{S}_m = \frac{\rho_m}{\rho_{0_m}} \frac{G_m \theta}{\theta_0} \left(\frac{3}{\text{tr } \boldsymbol{B}^{-1}_{\kappa_{p_m(t)}}} - 1\right) \boldsymbol{I} + 2\mu_m \boldsymbol{D} \tag{77}$$

$$\frac{\mu_s}{G_{1s}} \overset{\nabla}{\boldsymbol{S}}_s + \frac{\rho_s}{\rho_{0_s}} \boldsymbol{S}_s = \frac{\rho_s}{\rho_{0_s}} G_{1s} \left(\frac{3}{\text{tr } \boldsymbol{B}^{-1}_{\kappa_{p_s(t)}}} \boldsymbol{I} + \frac{G_{2s}}{G_{1s}} \boldsymbol{B}_{\kappa_r}\right) \tag{78}$$

$$\frac{\partial c_m}{\partial t} = -\frac{\epsilon_m}{N_A h\nu} c_m^2 \boldsymbol{I} \tag{79}$$

The initial conditions for $\boldsymbol{v}, \boldsymbol{T}$, θ, I and ρ_i are given by

$$\boldsymbol{v}(\boldsymbol{x}, T_1) = \boldsymbol{v}_0(\boldsymbol{x}, T_1) \tag{80}$$

$$\boldsymbol{T}(\boldsymbol{x}, T_1) = \boldsymbol{T}_0(\boldsymbol{x}, T_1) \tag{81}$$

$$\theta(\boldsymbol{x}, T_1) = \theta_0(\boldsymbol{x}, T_1) \tag{82}$$

$$I(\boldsymbol{x}, T_1) = 0 \tag{83}$$

$$\rho_m(\boldsymbol{x}, T_1) = \rho_{0_m}(\boldsymbol{x}, T_1) \tag{84}$$

$$\rho_s(\boldsymbol{x}, T_1) = 0 \tag{85}$$

where $\boldsymbol{v}_0, \boldsymbol{T}_0$, θ_0 and ρ_{0_m} are the final conditions of the previous mold filling process and the density of the solid part of the mixture is zero since the fluid is completely melted.

The boundary conditions are given by

$$\boldsymbol{v} = \boldsymbol{0} \qquad \text{(at the mold)} \tag{86}$$

$$\rho \boldsymbol{v}(\boldsymbol{v} \cdot \hat{n}) = (\boldsymbol{T} - \boldsymbol{T}_{subs})\hat{n} \qquad \text{(at the substrate)} \tag{87}$$

$$-k(\text{grad } \theta) = \vec{q}_{\text{mold}} \qquad \text{(at the mold)} \tag{88}$$

$$-(\text{grad } \theta) \cdot \hat{n} = h_c A(\theta - \theta_{\text{air}}) \qquad \text{(at the substrate)} \tag{89}$$

$$I = I_0 \qquad \text{(at the mold)} \tag{90}$$

$$(\text{grad } I) \cdot \hat{n} = J_0 \qquad \text{(at the substrate)} \tag{91}$$

All the previous boundary conditions have a periodic condition implemented on the sides. .

6. Simplified model

The governing equations for phase change as posed in Section 5 are nonlinear and hard to solve. To simplify the problem and in an effort to obtain meaningful solutions, as the first step we will consider a simplified version of the general problem without

temperature changes (i.e., $\theta = \theta_0$) that can exhibit the basic viscoelastic behavior that we conjecture as appropriate for the phase change process. We will assume that the displacement gradient and its time rate to be small, that is

$$\left\| \frac{\partial \boldsymbol{u}}{\partial \mathbf{X}} \right\| \sim O(\varepsilon), \quad \left\| \frac{\partial^2 \boldsymbol{u}}{\partial \mathbf{X} \partial t} \right\| \sim O(\varepsilon) \tag{92}$$

that the left Cauchy stress tensors of both natural configurations of the melt and the solid portion of the mixture satisfy

$$\left\| \boldsymbol{B}_{\kappa_{p_i(t)}} - \boldsymbol{I} \right\| \sim O(\varepsilon) \tag{93}$$

that the phase change starts at time $t = T_1$

$$\boldsymbol{B}_{\kappa_r} = \boldsymbol{B} \tag{94}$$

and that the density of both the melt and solid parts satisfy

$$\rho_m + \rho_s = \rho_0, \quad 0 \le \rho_i \le \rho_0 \tag{95}$$

where ρ_0 is given and fixed.

With the previous simplifying assumptions the governing equations reduce to

$$\rho_0 \frac{d^2 \boldsymbol{u}}{dt^2} = \operatorname{div} \boldsymbol{\sigma} \tag{96}$$

$$\operatorname{div} \left(\frac{\partial \boldsymbol{u}}{\partial t} \right) = 0 \tag{97}$$

$$\frac{1}{c} \frac{\partial I}{\partial t} + \hat{r} \cdot \frac{\partial I}{\partial \mathbf{x}} + (a c_m + a_s c_s) I = 0 \tag{98}$$

$$\boldsymbol{\sigma} = -p \boldsymbol{I} + \boldsymbol{\sigma}_m + \boldsymbol{\sigma}_s \tag{99}$$

$$\rho_i = c_i M_i \tag{100}$$

and the constitutive equations are now given by

$$\boldsymbol{\sigma}_m = \left(\alpha \frac{\mu}{\lambda_1} \right) \boldsymbol{I} + \alpha \boldsymbol{\tau}_m \tag{101}$$

$$\boldsymbol{\sigma}_s = (1 - \alpha) \boldsymbol{\tau}_s \tag{102}$$

$$\lambda_1 \frac{\partial \boldsymbol{\tau}_m}{\partial t} + \alpha \boldsymbol{\tau}_m = 2\mu \frac{\partial \boldsymbol{\varepsilon}}{\partial t} \tag{103}$$

$$\lambda_2 \frac{\partial \boldsymbol{\tau}_s}{\partial t} + (1 - \alpha) \boldsymbol{\tau}_s = 2(1 - \alpha) G (\boldsymbol{I} + \boldsymbol{\varepsilon}) \tag{104}$$

$$\frac{\partial c_m}{\partial t} = -\frac{\epsilon_m}{N_A h \nu} c_m^2 I \tag{105}$$

where the displacement $\boldsymbol{u}$ is related to the velocity $\boldsymbol{v}$ by

$$\frac{d \boldsymbol{u}}{dt} = \boldsymbol{v} \tag{106}$$

$\boldsymbol{\varepsilon}(\boldsymbol{u})$, $\boldsymbol{\sigma}$, $\boldsymbol{\tau}$ are the linearized strain, Cauchy stress, extra stress tensors respectively, p the Lagrange multiplier as a consequence of the isochoricity of the motion of the mixture and λ_1, λ_2, μ, G the relaxation time of the melt the relaxation time of the solid and the shear modulus of the melt and solid constituents respectively.

Let us further assume that the density of each constituent depends only on time (i.e. $\rho_i = \rho_i(t)$), then we have that the evolution of the system is given by

$$\rho_0 \frac{d^2 \boldsymbol{u}}{dt^2} = -\operatorname{grad} p + \alpha \operatorname{div} \boldsymbol{\tau}_m + (1 - \alpha) \operatorname{div} \boldsymbol{\tau}_s \tag{107}$$

$$\operatorname{div} \boldsymbol{u} = 0 \tag{108}$$

$$\frac{1}{c} \frac{\partial I}{\partial t} + \hat{r} \cdot \frac{\partial I}{\partial \mathbf{x}} + \left(a_m \frac{\rho_m}{M_m} + a_s \frac{\rho_s}{M_s} \right) I = 0 \tag{109}$$

$$\frac{d}{dt} \left(\frac{\rho_m}{M_m} \right) = -\frac{\epsilon_m}{N_A h \nu} \left(\frac{\rho_m}{M_m} \right)^2 I \tag{110}$$

where the differential equations describing the evolution of the Cauchy stress tensor can now be solved explicitly and written in the form

$$\begin{aligned} \boldsymbol{\tau}_m &= e^{-\frac{1}{\lambda_1} \int_{T_1}^t \alpha d\tau} \boldsymbol{\tau}_m|_{t=T_1} + \frac{2\mu}{\lambda_1} \int_{T_1}^t e^{-\frac{1}{\lambda_1} \int_s^t \alpha d\tau} \frac{\partial \boldsymbol{\varepsilon}}{\partial s} ds \\ &= e^{-\frac{1}{\lambda_1} \int_{T_1}^t \alpha d\tau} \frac{2\mu}{\lambda_1} \int_0^{T_1} e^{-\frac{T_1 - s}{\lambda_1}} \frac{\partial \boldsymbol{\varepsilon}}{\partial s} ds + \frac{2\mu}{\lambda_1} \int_{T_1}^t e^{-\frac{1}{\lambda_1} \int_s^t \alpha d\tau} \frac{\partial \boldsymbol{\varepsilon}}{\partial s} ds \end{aligned} \tag{111}$$

$$\boldsymbol{\tau}_s = -p_s \boldsymbol{I} + \frac{2G}{\lambda_2} \int_{T_1}^t (1 - \alpha) e^{-\frac{1}{\lambda_2} \int_s^t (1 - \alpha) d\tau} (\boldsymbol{I} + \boldsymbol{\varepsilon}) ds \tag{112}$$

Furthermore, we will also assume that the process is bi-dimensional in the sense that any cross section perpendicular to the axis of the mold will have the same strain/stress distribution. By the use of a cylindrical coordinate system aligned with the mold roller, we clearly see that the conservation of linear momentum and mass can be modeled by the equations

$$\rho_0\left[\frac{\partial^2 \boldsymbol{u}}{\partial t^2} - 2(\omega\hat{e}_z)\times\frac{\partial \boldsymbol{u}}{\partial t} - \omega^2(\boldsymbol{u}+\boldsymbol{r})\right] = -\text{grad } p + \alpha \text{ div } \boldsymbol{\tau}_m + (1-\alpha)\text{ div } \boldsymbol{\tau}_s \tag{113}$$

$$\text{div } \boldsymbol{\tau}_m = \frac{\mu}{\lambda_1} e^{-\frac{1}{\lambda_1}\int_{T_1}^{t}\alpha d\tau}\int_0^{T_1} e^{-\frac{T_1-s}{\lambda_1}}\frac{\partial}{\partial s}(\Delta \boldsymbol{u})ds + \frac{\mu}{\lambda_1}\int_{T_1}^{t} e^{-\frac{1}{\lambda_1}\int_s^t \alpha d\tau}\frac{\partial}{\partial s}(\Delta \boldsymbol{u})ds$$

$$\text{div } \boldsymbol{\tau}_s = \frac{G}{\lambda_2}\int_{T_1}^{t}(1-\alpha)e^{-\frac{1}{\lambda_2}\int_s^t(1-\alpha)d\tau}(\Delta \boldsymbol{u})ds$$

$$\text{div } \boldsymbol{u} = 0 \tag{114}$$

$$\hat{r}\cdot\frac{\partial I}{\partial \mathbf{x}} + \rho_0\left[\alpha\frac{a_m}{M_m} + (1-\alpha)\frac{a_s}{M_s}\right] I = 0 \tag{115}$$

$$\frac{\partial \alpha}{\partial t} + \frac{\epsilon_m \rho_0}{N_A h\nu M_m}\alpha^2 I = 0 \tag{116}$$

where the second and third terms inside the brackets on the left hand side of Eq. (113) are the Coriolis and the centripetal accelerations respectively.

Next having in mind that

$$R_0 \le r \le R_0 + H, \quad 0 \le \theta \le \frac{L}{R_0+H}, \quad T_1 \le t \le T_2 - T_1 \tag{117}$$

let us define the non-dimensional variables

$$\bar{\theta} = \frac{R_0+H}{L}\theta, \qquad \bar{r} = \frac{R_0 - r}{H}, \qquad \bar{t} = \frac{t-T_1}{T_2-T_1}$$

$$\bar{u}_\theta = \frac{u_\theta}{L}, \qquad \bar{u}_r = \frac{u_r}{H}, \qquad \bar{p} = \frac{\lambda_1}{\mu}p$$

$$\bar{I} = \frac{I}{I_0}, \qquad \alpha = \frac{\rho_m}{\rho_0}, \qquad Wi = \frac{\lambda_1 v_s(0)}{H}$$

$$De_1 = \frac{\lambda_1}{T_2-T_1}, \qquad De_2 = \frac{\lambda_2}{T_2-T_1}, \qquad Re = \frac{\rho_{0_m} v_s(0) H}{\mu}$$

$$K = \frac{G\lambda_1}{\mu}, \qquad P_1 = \frac{H\rho_{0_m} a_m}{M_m}, \qquad P_2 = \frac{(T_2-T_1)\epsilon_m \rho_{0_m} I_0}{N_A h\nu M_m}$$

where Wi is the Weissenberg number, De_1 and De_2 are the Deborah numbers of the melt and the solid respectively, Re is the Reynolds number of the mixture, K is the ratio between solid and fluid shear, P_1 and P_2 are nondimensional numbers coming from the photo-chemistry of the mixture and $v_s(t)$ is given by

$$v_s(0) = \frac{d}{dt}\left(u_s(t)\right)\Big|_{t=0} \tag{118}$$

where the displacement function of the substrate[1] is defined as

$$u_s(t) = R_o\left[\left(1-\frac{H-h}{R_o}\right)\cos(\omega t) + \sqrt{1-\left(1-\frac{H-h}{R_o}\right)^2}\sin(\omega t) - 1\right] + H - h. \tag{119}$$

With these definitions and taking into account once more the nano-scale of the features we can show that the differential operators in cylindrical coordinates are approximately the same as their Cartesian counterparts, and that the componentwise conservation of linear momentum and mass are given by

$$\frac{ReDe_1^2}{Wi}\left[\frac{\partial^2 \bar{u}_\theta}{\partial \bar{t}^2} + \pi\left(\frac{H}{L}\right)\frac{\partial \bar{u}_r}{\partial \bar{t}} - (\pi/2)^2\bar{u}_\theta\right] = \alpha\left[\frac{De_1}{2De_0}e^{-\frac{1}{De_1}\int_0^{\bar{t}}\alpha d\bar{s}}\frac{\partial}{\partial \bar{s}}(\bar{\Delta}\bar{u}_{0_\theta}) + \int_0^{\bar{t}} e^{-\frac{1}{De_1}\int_{\bar{s}}^{\bar{t}}\alpha d\bar{s}}\frac{\partial}{\partial \bar{s}}(\bar{\Delta}\bar{u}_\theta)d\bar{s}\right]$$
$$+ (1-\alpha)\left[\frac{K}{De_2}\int_0^{\bar{t}}(1-\alpha)e^{-\frac{1}{De_2}\int_{\bar{s}}^{\bar{t}}(1-\alpha)d\bar{s}}(\bar{\Delta}\bar{u}_\theta)d\bar{s}\right] - \left(\frac{H}{L}\right)^2\frac{\partial \bar{p}}{\partial \bar{\theta}} \tag{120}$$

$$\frac{ReDe_1^2}{Wi}\left[\frac{\partial^2 \bar{u}_r}{\partial \bar{t}^2} - \pi\left(\frac{L}{H}\right)\frac{\partial \bar{u}_\theta}{\partial \bar{t}} - (\pi/2)^2(\bar{u}_r + \frac{R_0}{H} - \bar{r})\right] = \alpha\left[\frac{De_1}{2De_0}e^{-\frac{1}{De_1}\int_0^{\bar{t}}\alpha d\bar{s}}\frac{\partial}{\partial \bar{s}}(\bar{\Delta}\bar{u}_{0_r}) + \int_0^{\bar{t}} e^{-\frac{1}{De_1}\int_{\bar{s}}^{\bar{t}}\alpha d\bar{s}}\frac{\partial}{\partial \bar{s}}(\bar{\Delta}\bar{u}_r)d\bar{s}\right]$$
$$+ (1-\alpha)\left[\frac{K}{De_2}\int_0^{\bar{t}}(1-\alpha)e^{-\frac{1}{De_2}\int_{\bar{s}}^{\bar{t}}(1-\alpha)d\bar{s}}(\bar{\Delta}\bar{u}_r)d\bar{s}\right] + \frac{\partial \bar{p}}{\partial \bar{r}} \tag{121}$$

[1] for more details refer to Gomez-Constante et al. (2019)

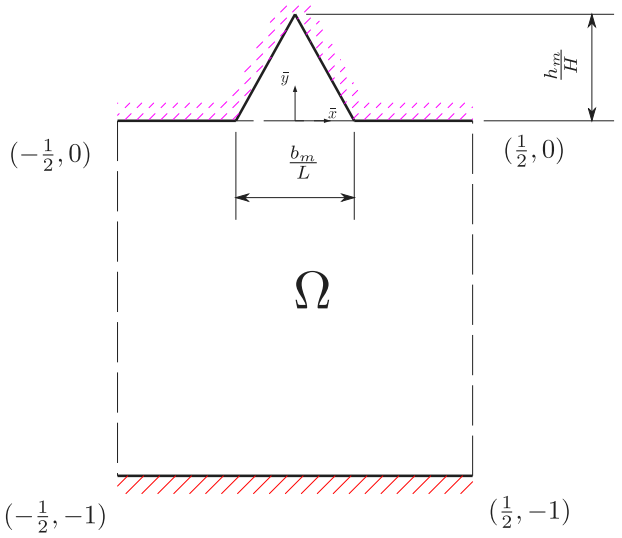

Fig. 8. Spatial domain for numerical computations.

$$\frac{\partial \bar{u}_\theta}{\partial \bar{\theta}} - \frac{\partial \bar{u}_r}{\partial \bar{r}} = 0 \tag{122}$$

$$-\left(\frac{H}{L}\right)\sin\bar{\phi}_r \frac{\partial \bar{I}}{\partial \bar{\theta}} + \cos\bar{\phi}_r \frac{\partial \bar{I}}{\partial \bar{r}} + P_1\left[(1-\frac{a_s M_m}{a_m M_s})\alpha + \frac{a_s M_m}{a_m M_s}\right]\bar{I} = 0 \tag{123}$$

$$\frac{\partial \alpha}{\partial \bar{t}} + P_2\alpha^2\bar{I} = 0 \tag{124}$$

where the nondimensional angles $\bar{\phi}_l$ and $\bar{\phi}_r$ are given by

$$\sin\bar{\phi}_l = \frac{\left|\cos(\frac{\pi}{2}\bar{r}) - \sin(\frac{\pi}{2}\bar{r})\right|}{\sqrt{(1-\sin(\frac{\pi}{2}\bar{r}))^2 + (1-\cos(\frac{\pi}{2}\bar{r}))^2}} \tag{125}$$

$$\sin\bar{\phi}_r = \frac{n_a}{n_f}\sin\bar{\phi}_l \tag{126}$$

the non-dimensional Laplacian operator ($\bar{\Delta}$) operating on a nondimensional function $\bar{v}$ is defined as

$$\bar{\Delta}\bar{v} = \left(\frac{H}{L}\right)^2 \frac{\partial^2 \bar{v}}{\partial \bar{\theta}^2} + \frac{\partial^2 \bar{v}}{\partial \bar{r}^2}. \tag{127}$$

It is worth mentioning that since the last two equations defining the photo-chemistry of the problem do not depend on $\bar{u}_\theta$, $\bar{u}_r$ nor $\bar{p}$, they can be solved independently of the others and then used in the other equations.

6.1. Mathematical model

Let $\Omega = (-\frac{1}{2},\frac{1}{2})\times(-1,0) \subset \mathbb{R}^2$ be the spatial domain, and $I_t = (0,1) \subset \mathbb{R}$ the time interval in which the available time for phase change takes place (Fig. 8). Set $\Omega_t = \Omega \times I_t$ as the space–time domain. The process that changes the viscoelastic fluid into a viscoelastic solid is then given by the quasi-linear system of partial differential equations

$$\frac{ReDe_1^2}{Wi}\left[\frac{\partial^2 \bar{u}_\theta}{\partial \bar{t}^2} + \pi\left(\frac{H}{L}\right)\frac{\partial \bar{u}_r}{\partial \bar{t}} - (\pi/2)^2\bar{u}_\theta\right] - \alpha\left[\frac{De_1}{2De_0}e^{-\frac{1}{De_1}\int_0^{\bar{t}}\alpha d\bar{s}}\frac{\partial}{\partial \bar{s}}(\bar{\Delta}\bar{u}_{0_\theta}) + e^{-\frac{1}{De_1}\int \alpha d\bar{\tau}} * d(\bar{\Delta}\bar{u}_\theta)\right]$$
$$-(1-\alpha)K\left[d\left(e^{-\frac{1}{De_2}\int(1-\alpha)d\bar{\tau}}\right) * \bar{\Delta}\bar{u}_\theta\right] + \left(\frac{H}{L}\right)^2\frac{\partial \bar{p}}{\partial \bar{\theta}} = 0 \tag{128}$$

$$\frac{ReDe_1^2}{Wi}\left[\frac{\partial^2 \bar{u}_r}{\partial \bar{t}^2} - \pi\left(\frac{L}{H}\right)\frac{\partial \bar{u}_\theta}{\partial \bar{t}} - (\pi/2)^2\bar{u}_r\right] - \alpha\left[\frac{De_1}{2De_0}e^{-\frac{1}{De_1}\int_0^{\bar{t}}\alpha d\bar{s}}\frac{\partial}{\partial \bar{s}}(\bar{\Delta}\bar{u}_{0_r}) + e^{-\frac{1}{De_1}\int \alpha d\bar{\tau}} * d(\bar{\Delta}\bar{u}_r)\right]$$
$$-(1-\alpha)K\left[d\left(e^{-\frac{1}{De_2}\int(1-\alpha)d\bar{\tau}}\right) * \bar{\Delta}\bar{u}_r\right] - \frac{\partial \bar{p}}{\partial \bar{r}} = \frac{ReDe_1^2}{Wi}(\pi/2)^2(\frac{R_0}{H} - \bar{r}) \tag{129}$$

$$\frac{\partial \bar{u}_\theta}{\partial \bar{\theta}} - \frac{\partial \bar{u}_r}{\partial \bar{r}} = 0 \tag{130}$$

$$-\left(\frac{H}{L}\right)\sin\bar{\phi}_r\frac{\partial \bar{I}}{\partial \bar{\theta}} + \cos\bar{\phi}_r\frac{\partial \bar{I}}{\partial \bar{r}} + P_1\left[(1-\frac{a_s M_m}{a_m M_s})\alpha + \frac{a_s M_m}{a_m M_s}\right]\bar{I} = 0 \tag{131}$$

$$\frac{\partial \alpha}{\partial \bar{t}} + P_2 \alpha^2 \bar{I} = 0 \tag{132}$$

with initial conditions given by:

$$\bar{u}_{\bar{\theta}} = \bar{u}_{\bar{x}}, \qquad \frac{\partial \bar{u}_{\bar{\theta}}}{\partial \bar{t}} = \bar{v}_{\bar{x}} \tag{133}$$

$$\bar{u}_{\bar{r}} = \bar{u}_{\bar{y}}, \qquad \frac{\partial \bar{u}_{\bar{r}}}{\partial \bar{t}} = \bar{v}_{\bar{y}} \tag{134}$$

$$\bar{I} = 0 \tag{135}$$

$$\alpha = 1 \tag{136}$$

periodic boundary conditions on the sides of the spatial domain, and with upper no-slip boundary conditions on the displacements. For the lower boundary conditions on displacements we will split this into two cases, namely the traction boundary conditions given by

$$\begin{aligned} &-\bar{p} + \alpha \left[1 + \frac{De_1}{De_0} e^{-\frac{1}{De_1}\int_0^{\bar{t}} \alpha d\bar{s}} \frac{\partial}{\partial \bar{s}} \left(\frac{\partial \bar{u}_{0_r}}{\partial \bar{r}} \right) + 2e^{-\frac{1}{De_1}\int \alpha d\bar{\tau}} * d\left(\frac{\partial \bar{u}_r}{\partial \bar{r}} \right) \right] \\ &+ 2K(1-\alpha) \left[d\left(e^{-\frac{1}{De_2}\int (1-\alpha) d\bar{\tau}} \right) * \frac{\partial \bar{u}_r}{\partial \bar{r}} + \left(1 - e^{-\frac{1}{De_2}\int_0^{\bar{t}} (1-\alpha) d\bar{s}} \right) \right] = \frac{n_{\text{web}} \lambda_1}{A_{\text{web}} \mu} \end{aligned} \tag{137}$$

$$\frac{\partial \bar{u}_\theta}{\partial \bar{t}} = 0 \tag{138}$$

where n_{web} is the reaction force due to the tension of the web in the normal direction to the substrate and A_{web} is the area of contact between the substrate and the mixture or the non-slip boundary conditions given by

$$\frac{\partial \bar{u}_r}{\partial \bar{t}} = 0 \tag{139}$$

$$\frac{\partial \bar{u}_\theta}{\partial \bar{t}} = 0. \tag{140}$$

6.2. Numerical scheme

For numerical simulations we use what is know in the literature as the Finite Difference Marker and Cell (MAC) Scheme for free surfaces (Harlow & Welch, 1965). This method consists in discretizing the differential and integral operators in order to generate a mesh on a rectangular domain (Fig. 9) in a way that the discretized equations for displacement and pressure satisfy what is called the inf-sup condition, which is a necessary and sufficient condition for existence and uniqueness of solutions to the system of PDEs defining the mechanical behavior of the problem (Boffi, Brezzi, Fortin, et al., 2013). In addition the MAC scheme enables us to have boundary conditions only for displacement which are the natural boundary conditions that arise from the physics of the problem.

In order to simplify things even more, we separated the system of equations with regard to the mechanical and photo-chemical behavior, that is, we will solve the photochemical reaction (Eqs. (131) and (132)) to then use the mass fraction of the melt previously obtained to determine the mechanical response of the mixture (Eqs. (128)–(130)). By solving the problem this way we avoid dealing with non-linear equations that arise as a consequence of the conservation of linear momentum and mass and isolate the nonlinearities of the photo-chemistry of the problem in a simpler system of PDE. The numerical scheme to find the mass fraction of the melt and the non-dimensional intensity of the light is a straightforward quasilinear finite difference scheme so its discussion is not relevant. However, the numerical scheme to find the non-dimensional displacements and pressure are worth discussing.

Let $h = 1/(N-1)$ and $\tau = 1/(m-1)$ be the space and time steps of the discrete problem. At the node i at time $(n+2)\tau$ (Fig. 10) the integral and differential operators involving the horizontal displacement $\bar{u}_x$ are given by

$$\frac{\partial \bar{u}_\theta}{\partial \bar{t}} \approx \frac{u_i^{n+2} - 2u_i^{n+1} + u_i^n}{\tau^2} \tag{141}$$

$$\begin{aligned} \int_0^{\bar{t}} e^{-\frac{\bar{t}-s}{De}} \frac{\partial}{\partial s} \left[\left(\frac{H}{L} \right)^2 \frac{\partial^2 \bar{u}_\theta}{\partial \bar{\theta}^2} + \frac{\partial^2 \bar{u}_\theta}{\partial \bar{r}^2} \right] ds &= \sum_{j=1}^{n+2} \int_{(j-1)\tau}^{j\tau} e^{-\frac{(n+2)\tau - s}{De}} \frac{\partial}{\partial s} \left[\left(\frac{H}{L} \right)^2 \frac{\partial^2 \bar{u}_\theta}{\partial \bar{\theta}^2} + \frac{\partial^2 \bar{u}_\theta}{\partial \bar{r}^2} \right] ds \\ &\approx \sum_{j=1}^{n+2} e^{-\frac{(n-j+5/2)\tau}{De}} \left[\left(\frac{H}{L} \right)^2 \frac{\partial^2 \bar{u}_\theta}{\partial \bar{\theta}^2} + \frac{\partial^2 \bar{u}_\theta}{\partial \bar{r}^2} \right]_i^j \\ &\quad - \sum_{j=1}^{n+2} e^{-\frac{(n-j+5/2)\tau}{De}} \left[\left(\frac{H}{L} \right)^2 \frac{\partial^2 \bar{u}_\theta}{\partial \bar{\theta}^2} + \frac{\partial^2 \bar{u}_\theta}{\partial \bar{r}^2} \right]_i^{j-1} \end{aligned} \tag{142}$$

where the elliptic operator is approximated as

$$\left[\left(\frac{H}{L} \right)^2 \frac{\partial^2 \bar{u}_\theta}{\partial \bar{\theta}^2} + \frac{\partial^2 \bar{u}_\theta}{\partial \bar{r}^2} \right]_i^j \approx \frac{1}{h^2} \left\{ \left(\frac{H}{L} \right)^2 u_{i+1}^j - 2\left[\left(\frac{H}{L} \right)^2 + 1 \right] u_i^j + \left(\frac{H}{L} \right)^2 u_{i-1}^j + u_{i+N}^j + u_{i-N}^j \right\} \tag{143}$$

notice that because of our choice of non-dimensional scales we are able to use the same spatial step for both space directions. By a similar process, we can discretize the rest of the differential equations to ultimately see that the photochemistry of phase change

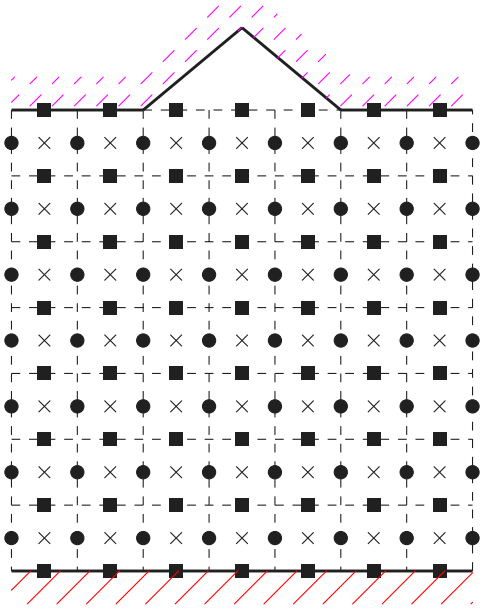

Fig. 9. MAC mesh showing nodes for displacement in horizontal direction (circles), vertical direction (squares) and pressure (X marks). The vertices of the dashed squares are the nodes for light intensity and mass fraction of the melt calculations.

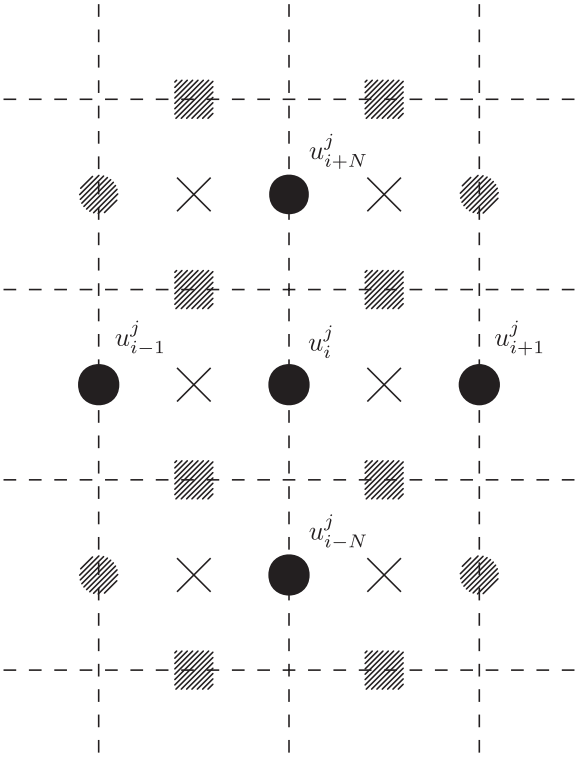

Fig. 10. Nodes involved in the space discretization of the horizontal displacement.

model is described by the nonlinear system of equations:

$$M_1 \bar{\boldsymbol{I}}^{n+1} + K_1(\boldsymbol{\alpha}^{n+1})\bar{\boldsymbol{I}}^{n+1} = \mathbf{0} \tag{144}$$

$$M_2\boldsymbol{\alpha}^{n+1} + K_2(\bar{\boldsymbol{I}}^{n+1})\boldsymbol{\alpha}^{n+1} = \mathbf{0} \tag{145}$$

where M_1, M_2, K_1 and K_2 are the sparse matrices defining the radiative transfer function and the response of the material with respect to the intensity of the light, and the linear system of equations

$$A_1(\boldsymbol{\alpha})\boldsymbol{u}^{n+2} + A_2(\boldsymbol{\alpha})\boldsymbol{v}^{n+2} + B_1\boldsymbol{p}^{n+1} = \boldsymbol{b}_1^{n+1} \tag{146}$$

$$A_3(\boldsymbol{\alpha})\boldsymbol{u}^{n+2} + A_4(\boldsymbol{\alpha})\boldsymbol{v}^{n+2} + B_2\boldsymbol{p}^{n+1} = \boldsymbol{b}_2^{n+1} \tag{147}$$

$$C_1\boldsymbol{u}^{n+2} + C_2\boldsymbol{v}^{n+2} + \varepsilon\boldsymbol{p}^{n+1} = \mathbf{0} \tag{148}$$

where A_1, A_2, A_3, A_3, B_1, B_2, C_1 and C_2 are the sparse matrices defining the finite difference approximations of the integral and differential operators. Notice that the matrices A_i depend on the mass fraction of the melt, but since it has already been calculated in the photochemistry equations, the second system of equations is linear in its variables. In addition, to avoid the restriction on the functional space to which the pressure field belongs, (given by the incompressible mixture assumption) a perturbation in the conservation of mass has been added, where ε is as small as possible to avoid accumulation of numerical errors.

7. Results and discussion

In order to carry out some numerical simulations, a numerical scheme was implemented in MATLAB®. The restrictions imposed by the isochoric motion assumption of the mixture affected the pressure terms and ultimately the displacement field. For that reason we added a perturbation of the pressure in the conservation of mass to help alleviate that pressure restriction and improve the numerical stability of the simulations. By doing so we were able to decouple the photochemical behavior from the thermomechanical behavior and solve them independently.

7.1. Effect of UV-light intensity

To understand how the UV-light intensity and the mass fraction of the melt affect the photochemistry of the problem, we ran some numerical simulations of their behavior independently of the thermomechanics. From the results we concluded that both the UV-light intensity and the mass fraction of the melt change so little across the domain that it is very accurate to assume that the mass fraction of the melt is spatially uniform and that it only evolves in time. This assumption is what enabled us to take the mass fraction of the melt as a function of time only in the thermomechanical behavior, transforming it into a linear integro-differential system of equations.

Fig. 11 depicts the mass fraction of the melt for different UV light sources. It is clear that the higher the intensity of the UV-light source, the higher the amount of melt being converted into solid. However, it is important to note that the higher the UV-light intensity the higher the amount of heat being irradiated to the surroundings which could possibly affect the isothermal assumption or even the behavior of the phase change process by the amount of energy present in form of heat being absorbed by the mold roller and on the surroundings.

7.2. Effect of boundary conditions

In order to understand how the timeline of the phase change process works we need to understand how the mold filling process works. It starts from an undeformed fluid film at rest which is then squeezed against a mold cavity by the relative motion between the mold roller and the nip roller in order to fill the mold cavity with it. We will assume that the material properties and process parameters are such that the mold filling process has been successfully performed.[2] The final displacement and pressure field of the mold filling process are in fact the initial displacement and pressure field in the phase change process as it was mentioned before. Since photochemistry only takes place in the phase change process, both the mass fraction of the melt and the intensity of the light remain constant throughout the mold filling process, meaning that the laws that govern their behavior are identically zero.

For the sake of completeness in our analysis, both traction and no-slip boundary conditions have been individually considered in the model. In a complete nonlinear model, these two boundary conditions are a single nonlinear combination which represents the conservation of Linear Momentum on the boundary. Fig. 12 depicts the initial and final states of mold filling (upper left and right respectively) and the two possible outcomes of the phase change process. In the first scenario (lower left), the substrate (lower black line) is subject to traction boundary conditions only. This traction force on the boundary is at equilibrium with the external radial (vertical in one mold feature) reaction coming from the tension of the substrate web that keeps the mixture inside the mold cavity. Notice that the vertical fibers on the sides push down to about their original positions whereas the vertical fibers at the center portion of the substrate are pulled up the direction of the mold cavity which is consistent with how the vertical fibers are deformed in the mold filling process. In the second scenario (lower right), the substrate boundary is kept fixed at the same position as the final state of mold filling (upper right) and the boundary condition is given in terms of the classic non-slip condition. In this case, we notice that the recoiling happens sideways since the displacement restriction prevents any vertical motion. We also notice that the mesh fiber structure looks more deformed compared to the traction only boundary condition. In the real manufacturing process we expect to have a combination of both scenarios: the recoiling of the substrate boundary condition due to the internal energy

[2] To understand what could go wrong with mold filling, the interested reader is referred to Gomez-Constante et al. (2020).

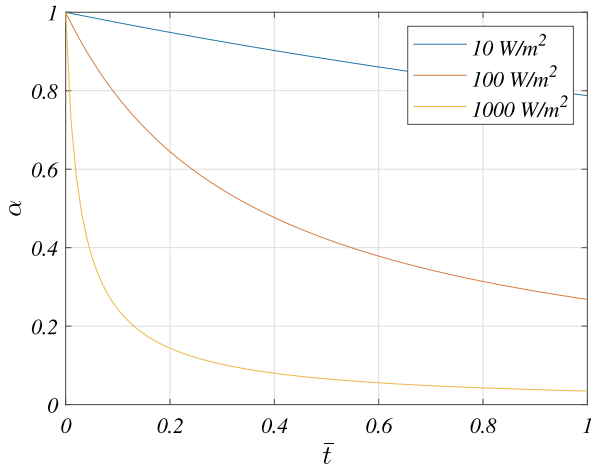

Fig. 11. Nondimensional mass fraction of the melt as they evolve in time for different UV-light intensities at the boundary.

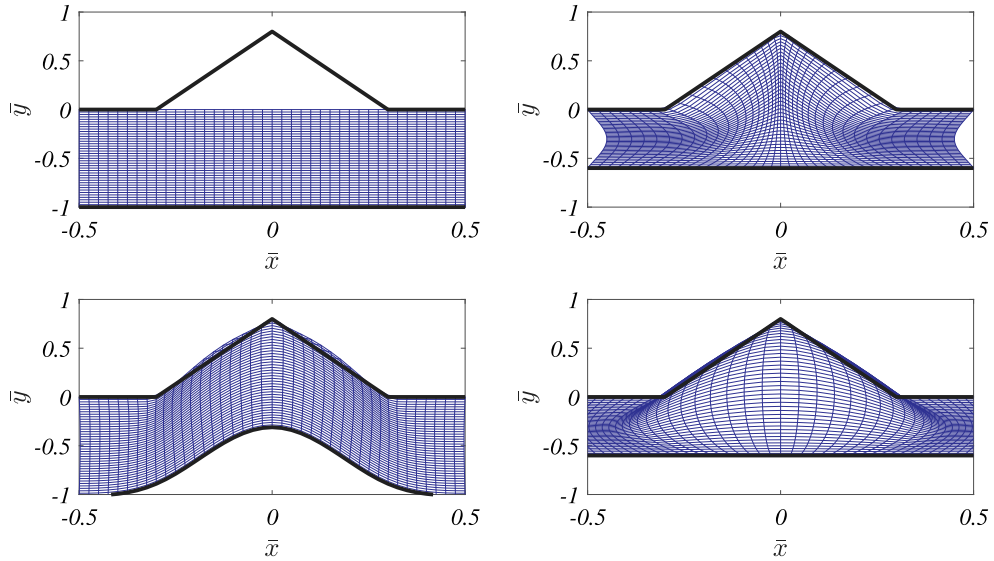

Fig. 12. Mixture film (blue fiber mesh) and mold/substrate boundaries (solid black lines) on mold filling and phase change processes for one feature. The mixture starts as a melt at rest (upper left), then the lower boundary moves up causing the mold cavity to be filled if the material and process parameters are adequate (upper right) which also determines the initial state of phase change. From this point on, if the traction conditions are enforced then the fluid film recoils back and the lower boundary is deformed (lower left), but if no-slip boundary conditions are enforced, then the recoiling happens sideways (lower right).

stored in the mold filling process and the substrate boundary remaining flat due to the higher relative stiffness of the web substrate. In addition, it must be mentioned that even though both mold filling and phase change processes were modeled as non-dimensional problems, the time scale in which phase change takes place is several orders of magnitude greater than the time scale of mold filling. What this effectively means is that the mold filling process happens so fast that it is virtually an instantaneous process with respect to the phase change process, regardless of the web speed.

Fig. 13 shows the Frobenius norm of strain and extra stress as well as pressure distribution across the nondimensional domain of the feature at the end of phase change when considering the traction boundary condition. It is clear that for most of the domain, the strain and extra stress are very low except for the mold roller boundary. That can be explained by the fact that the fibers in contact with the mold roller do not slip maintaining the strain they had at the moment of contact (at the mold filling process). As for pressure, the values clearly show that it is basically back to zero.

Fig. 14 shows the Frobenius norm of strain and extra stress as well as pressure distribution across the nondimensional domain of the feature at the end of phase change when considering the displacement boundary condition. In this case, it is clear that the strain is much higher than for the previous boundary conditions, specially around the upper and lower boundaries. In addition, we notice that the pressure values are several orders of magnitude higher that the values compared to the traction boundary conditions.

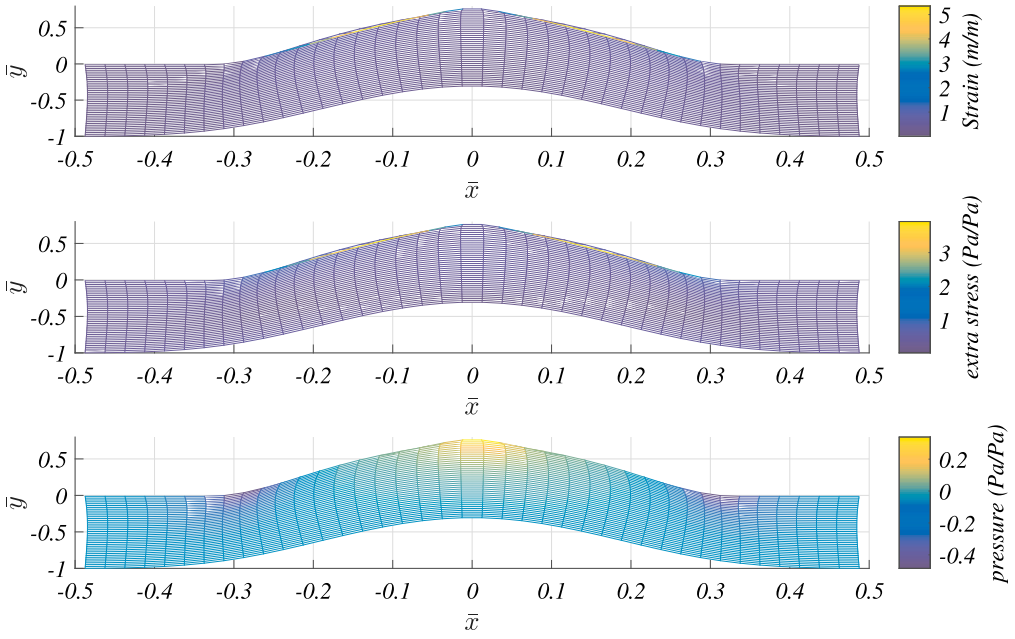

Fig. 13. Nondimensional Frobenius norm of strain, extra stress and pressure distribution at the end of phase change.

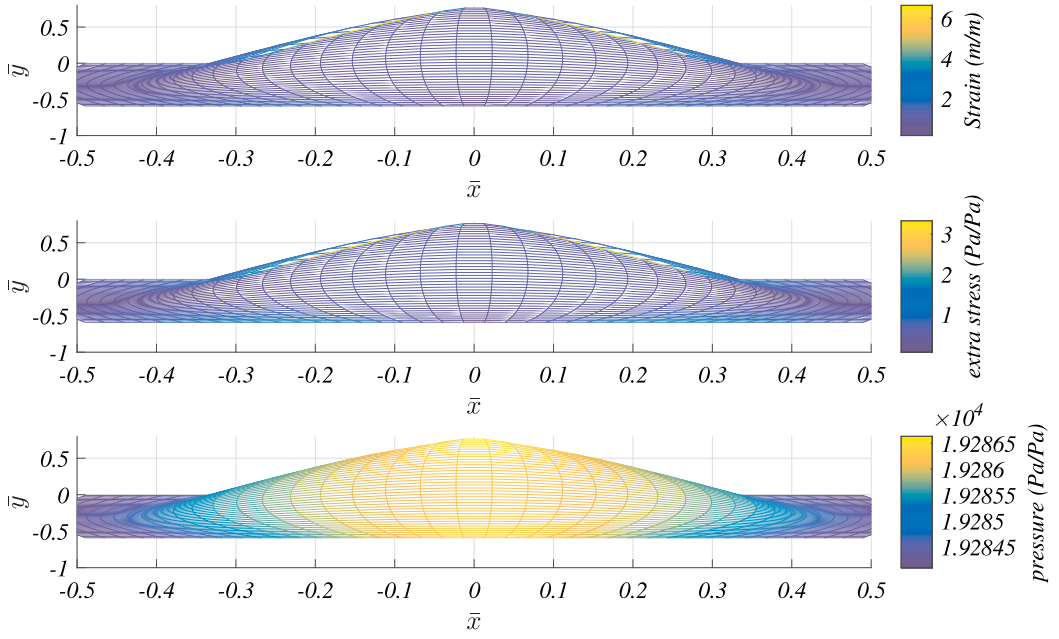

Fig. 14. Nondimensional Frobenius norm of strain, extra stress and pressure distribution at the end of phase change.

7.3. Effect of web speed

In this section of our analysis, we will use both boundary conditions previously described and analyzed and compare their respective effects in order to have a more general idea on what happens in the nonlinear case when the boundary condition at the substrate is given by the conservation of Linear Momentum.

Fig. 15 depicts the $L^2(\Omega)$ norm of the extra stress, strain, pressure and the mass fraction of the melt as they evolve in nondimensional time at the web speeds of 1 m/min and 10 m/min. In the extra stress we see a sudden jump at the beginning of the phase change process consistent with the instantaneous mold filling process at both web speeds to then relax to lower values for both boundary conditions. Notice that the higher the web speed the higher the initial stress and that there is a little stress recovery at

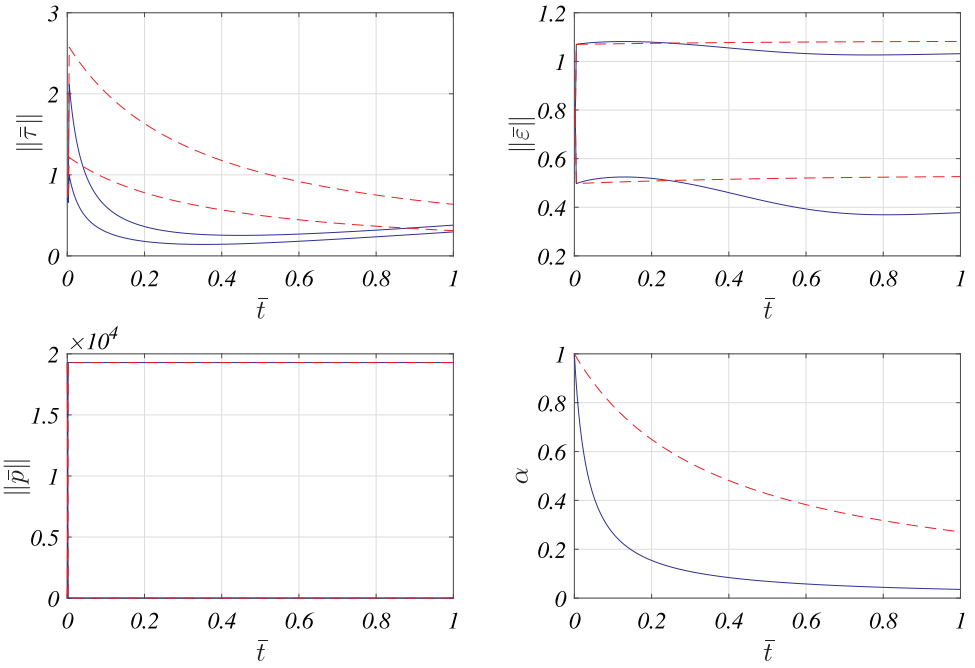

Fig. 15. $L^2(\Omega)$ norm of extra stress, strain and pressure, and mass fraction of the melt for both traction (higher value) and displacement (lower value) boundary conditions as they evolve in time at web speeds of 1 m/min (solid blue) and 10 m/min (dashed red).

lower web speeds consistent with the solid behavior becoming more dominant as the mixture changes phase. In addition, we notice that even though the traction boundary condition has lower values, its time evolution exhibits the same behavior. In the figure which depicts the strain, we again notice a sudden jump during the mold filling process to two high values corresponding to the different boundary conditions, that then remains about the same for the rest of the process. In this case, we notice that the higher the web speed the less the strain relaxes, consistent with the higher stress values and the reduced amount of time available for relaxation. As for the pressure, we see that its value drops back to zero for traction boundary conditions whereas for the displacement boundary conditions it jumps to a high value and stays approximately constant for the rest of the process, which is consistent with what we expect. Notice that this behavior is approximately the same regardless of the web speed. Finally, the mass fraction of the melt shows that the amount of melt decreases steadily (thus the amount of solid increases at the same rate) for both web speeds being faster and higher the amount of melt being converted into solid for lower web speeds, as expected.

8. Conclusions and future work

From the model development and analyses of the phase change sub-process, it is clear that the most important factors affecting phase change are the intensity of the UV-light source and web speed. Since our interest is to increase the throughput of the manufacturing process and based on the simulations we clearly see that any increase of the web speed is accompanied by a detriment of the amount of melt being converted into solid. Therefore, in order to increase the web speed we could potentially increase the intensity of the UV-light source, maximize the wrap angle, etc. to compensate the decrease of the amount of melt being converted into solid.

We can also conclude that the mold filling process is an instantaneous process with respect to phase change regardless of the web speed. Because of this, the elastic behavior will be dominant. However, if we can guarantee that the material properties and process parameters are such that the mold cavity will be adequately filled with the melt, then its impact on phase change is not significant.

With respect to numerical simulations, the isochoric motion assumption enforced on the mixture helps decoupling the photochemistry from the thermomechanical behavior making computations much easier. However, this additional assumption comes at the expense of constraining the functional space to which the pressure fields belong. The perturbation in the conservation of mass helps relaxing this constraint but it also inserts a small amount of error in the computations.

The following are potential directions that we will pursue on this topic in the near future.

1. We plan to conduct focused experiments to corroborate the key features of the model as well as to corroborate the model conclusions from the numerical simulations. These will include testing with various patterns and feature sizes and resin materials on a R2R UV-NIL testbed. We will also design and conduct material tests that can be used to obtain the resin material constants needed for optimizing the transport and process conditions for improving pattern quality. Some of the

material parameters can be obtained from the product manuals of the manufacturers of these resin films and substrates. However, some are not available, for example, stress relaxation time and surface tension; we plan to run some stress relaxation and surface tension experiments in the near future to obtain these parameters. Further, we have observed during R2R NIL experiments that the photochemical reactions associated with the resin coating material we have used are highly exothermal. Therefore, we also have to design experiments to evaluate whether there is a significant change in material parameters due to the temperature changes observed during UV light irradiation.

2. Investigate the effect of relaxing some or all of the linearizing assumptions, the isochoric motion of the mixture, and considering the general problem of interaction between photochemistry and thermomechanics. The general nonlinear problem is difficult to solve numerically because of the occurrence of stagnation points and zones where the stresses are very high resulting in fast accumulation of numerical errors. Currently, there are no available stable numerical methods for solving the general nonlinear model. This is precisely what happens with the high Weissenberg number flow problems, and until we figure out a proper numerical scheme, linearizing the equations and restricting the solution to a narrow range around the operating point is the way to avoid this numerical problem.
3. A potential extension is to model the interaction between the mixture and substrate. To pursue this model extension, one could assume the substrate to behave as a nonlinear elastic solid with traction forces on the left and right boundaries due substrate tension.
4. Develop a model for the demolding sub-process, which will depend on the upstream conditions associated with the mold filling and phase change sub-processes. Analysis of the demolding sub-process model can provide conditions (namely material properties and process parameters) under which the patterned surface can be released from the mold.

Declaration of competing interest

The authors declare that they have no known competing financial interests or personal relationships that could have appeared to influence the work reported in this paper.

Acknowledgments

This work was supported in part by the National Science Foundation under the grant number 1635636. K. R. Rajagopal thanks the Office for Naval Research for support of his work.

References

Ahn, S. H., & Guo, L. J. (2009). Large-area roll-to-roll and roll-to-plate nanoimprint lithography: A step toward high-throughput application of continuous nanoimprinting. *ACS Nano*, *3*(8), 2304–2310.

Ahn, S. H., Miller, M., Yang, S., Ganapathisubramanian, M., Menezes, M., Singh, V., et al. (2013). High volume nanoscale roll-based imprinting using jet and flash imprint lithography. In *Nanoengineering: Fabrication, properties, optics, and devices X (vol. 8816)* (p. 881602). International Society for Optics and Photonics.

Atkin, R. J., & Craine, R. E. (1976). Continuum theories of mixtures: Basic theory and historical development. *The Quarterly Journal of Mechanics and Applied Mathematics*, *29*(2), 209–244.

Avrami, M. (1939). Kinetics of phase change. I General theory. *The Journal of Chemical Physics*, *7*(12), 1103–1112.

Avrami, M. (1940). Kinetics of phase change. II transformation-time relations for random distribution of nuclei. *The Journal of Chemical Physics*, *8*(2), 212–224.

Avrami, M. (1941). Granulation, phase change, and microstructure kinetics of phase change. III. *The Journal of Chemical Physics*, *9*(2), 177–184.

Baldoni, F., & Rajagopal, K. R. (1997). A continuum theory for the thermomechanics of solidification. *International Journal of Non-Linear Mechanics*, *32*(1), 3–20.

Bankoff, S. G. (1964). Heat conduction or diffusion with change of phase. In *Advances in chemical engineering (vol. 5)* (pp. 75–150). Elsevier.

Barot, G., Rao, I. J., & Rajagopal, K. R. (2008). A thermodynamic framework for the modeling of crystallizable shape memory polymers. *International Journal of Engineering Science*, *46*(4), 325–351.

Beckermann, C., Diepers, H. J., Steinbach, I., Karma, A., & Tong, X. (1999). Modeling melt convection in phase-field simulations of solidification. *Journal of Computational Physics*, *154*(2), 468–496.

Boffi, D., Brezzi, F., Fortin, M., et al. (2013). *Mixed finite element methods and applications (vol. 44)*. Springer.

Bowen, R. M. (1967). Toward a thermodynamics and mechanics of mixtures. *Archive for Rational Mechanics and Analysis*, *24*(5), 370–403.

Chandrasekhar, S. (2013). *Radiative transfer*. Courier Corporation.

Crank, J. (1956). *The mathematics of diffusion* (p. 347). Oxford: Clarendon Press.

Fasano, A., Kannan, K., Mancini, A., & Rajagopal, K. R. (2007). Modelling ziegler–natta polymerization in high pressure reactors. In *Material substructures in complex bodies* (pp. 206–237). Elsevier.

Gomez-Constante, J. P., Pagilla, P. R., & Rajagopal, K. R. (2019). Effect of the processing and transport parameters on mold filling in roll-to-roll nanoimprint lithography. In *Proceedings of the fifteenth international conference on web handling*.

Gomez-Constante, J. P., Pagilla, P. R., & Rajagopal, K. R. (2020). A thermomechanical description of the mold filling process in roll-to-roll nanoimprinting lithography. *Applications in Engineering Science*, *1*(1), Article 100001.

Gupta, S. C. (2017). *The classical Stefan problem: Basic concepts, modelling and analysis with quasi-analytical solutions and methods (vol. 45)*. Elsevier.

Harlow, F. H., & Welch, J. E. (1965). Numerical calculation of time-dependent viscous incompressible flow of fluid with free surface. *Physics of Fluids*, *8*(12), 2182–2189.

Hu, H., & Argyropoulos, S. A. (1996). Mathematical modelling of solidification and melting: A review. *Modelling and Simulation in Materials Science and Engineering*, *4*(4), 371.

Inanami, R., Ojima, T., Matsuki, K., Kono, T., & Nakasugi, T. (2012). Sub-100 nm pattern formation by roll-to-roll nanoimprint. In *Alternative lithographic technologies IV (vol. 8323)* (p. 83231J). International Society for Optics and Photonics.

Jain, A., & Bonnecaze, R. T. (2013). Fluid management in roll-to-roll nanoimprint lithography. *Journal of Applied Physics*, *113*(23), Article 234511.

Kannan, K., & Rajagopal, K. R. (2004). A thermomechanical framework for the transition of a viscoelastic liquid to a viscoelastic solid. *Mathematics and Mechanics of Solids*, *9*(1), 37–59.

Kannan, K., & Rajagopal, K. R. (2011). A thermodynamical framework for chemically reacting systems. *Zeitschrift für Angewandte Mathematik und Physik*, *62*(2), 331–363.
Kannan, K., Rao, I. J., & Rajagopal, K. R. (2002). A thermomechanical framework for the glass transition phenomenon in certain polymers and its application to fiber spinning. *Journal of Rheology*, *46*(4), 977–999.
Kim, N. W., Kim, K. W., & Sin, H. C. (2009). A mathematical model for slip phenomenon in a cavity-filling process of nanoimprint lithography. *Microelectronic Engineering*, *86*(11), 2324–2329.
Lamé, G., & Clapeyron, B. (1831). Mémoire sur la solidification par refroidissement d'un globe liquide. *Annales Chimie Physique*, *47*, 250–256.
Lee, S. H., Kim, H. N., Kwak, R. K., & Suh, K. Y. (2009). Effects of mold rising angle and polymer concentration in solvent-assisted molding. *Langmuir*, *25*(20), 12024–12029.
Lin, C. H., & Chen, R. (2008). Impacts of Mold geometries and imprinted resist thickness on velocity fields for nanoimprint lithography. *Japanese Journal of Applied Physics*, *47*(6S), 5197.
Long, K. N., Scott, T. F., Qi, H. J., Bowman, C. N., & Dunn, M. L. (2009). Photomechanics of light-activated polymers. *Journal of the Mechanics and Physics of Solids*, *57*(7), 1103–1121.
Mäkelä, T., Haatainen, T., & Ahopelto, J. (2011). Roll-to-roll printed gratings in cellulose acetate web using novel nanoimprinting device. *Microelectronic Engineering*, *88*(8), 2045–2047.
Matschuk, M., & Larsen, N. B. (2012). Injection molding of high aspect ratio sub-100 nm nanostructures. *Journal of Micromechanics and Microengineering*, *23*(2), Article 025003.
Moon, S., Cui, F., & Rao, I. J. (2015). Constitutive modeling of the mechanics associated with triple shape memory polymers. *International Journal of Engineering Science*, *96*, 86–110.
Rajagopal, K. R., & Srinivasa, A. R. (2000). A thermodynamic frame work for rate type fluid models. *Journal of Non-Newtonian Fluid Mechanics*, *88*(3), 207–227.
Rajagopal, K. R., & Tao, L. (1995). *Mechanics of mixtures (vol. 35)*. World Scientific.
Rao, I. J., & Rajagopal, K. R. (2001). A study of strain-induced crystallization of polymers. *International Journal of Solids and Structures*, *38*(6–7), 1149–1167.
Rao, I. J., & Rajagopal, K. R. (2002). A thermodynamic framework for the study of crystallization in polymers. *Zeitschrift für angewandte Mathematik und Physik ZAMP*, *53*(3), 365–406.
Rubinšteĭn, L. (2000). *The stefan problem (vol. 8)*. American Mathematical Soc.
Sodhi, J. S., Cruz, P., & Rao, I. J. (2015). Inhomogeneous deformations of light activated shape memory polymers. *International Journal of Engineering Science*, *89*, 1–17.
Sohn, K. J., Park, J. H., Lee, D. E., Jang, H. I., & Lee, W. I. (2013). Effects of the process temperature and rolling speed on the thermal roll-to-roll imprint lithography of flexible polycarbonate film. *Journal of Micromechanics and Microengineering*, *23*(3), Article 035024.
Sreejith, P., Kannan, K., & Rajagopal, K. R. (2021). A thermodynamic framework for additive manufacturing, using amorphous polymers, capable of predicting residual stress, warpage and shrinkage. *International Journal of Engineering Science*, *159*, Article 103412.
Thesen, M. W., Nees, D., Ruttloff, S., Rumler, M., Rommel, M., Schlachter, F., et al. (2014). Inkjetable and photo-curable resists for large-area and high-throughput roll-to-roll nanoimprint lithography. *Journal of Micro/Nanolithography, MEMS, and MOEMS*, *13*(4), Article 043003.
Thesen, M. W., Rumler, M., Schlachter, F., Grützner, S., Moormann, C., Rommel, M., et al. (2014). Enabling large area and high throughput roll-to-roll NIL by novel inkjetable and photo-curable NIL resists. In *Alternative lithographic technologies VI (vol. 9049)* (p. 90490H). International Society for Optics and Photonics.
Truesdell, C. (1962). Mechanical basis of diffusion. *The Journal of Chemical Physics*, *37*(10), 2336–2344.
Wang, J., Li, M., Qiu, J., & Zhou, Y. (2018). Filling angle and its effect on filling process in roll-to-roll ultraviolet imprint lithography. *Journal of Micromechanics and Microengineering*, *28*(3), Article 035011.
Wu, C. L., Sung, C. K., Yao, P. H., & Chen, C. H. (2013). Sub-15 nm linewidth gratings using roll-to-roll nanoimprinting and plasma trimming to fabricate flexible wire-grid polarizers with low colour shift. *Nanotechnology*, *24*(26), Article 265301.
Young, W. B. (2005). Analysis of the nanoimprint lithography with a viscous model. *Microelectronic Engineering*, *77*(3–4), 405–411.